Research Square

Preprints are preliminary reports that have not undergone peer review. They should not be considered conclusive, used to inform clinical practice, or referenced by the media as validated information.

Collision-Aware Coordination of Dual Drilling Manipulators Using RoboCompiler and Control Barrier Functions

Mehdi Heydari Shahna

mehdi.heydarishahna@tuni.fi

Tampere University

Tuomo Kivelä

Sandvik Mining and Construction Oy

Jouni Mattila

Tampere University

Research Article

Keywords: drilling-boom automation; dual-manipulator coordination; control barrier functions; hydraulic manipulators; collision avoidance; underground construction

Posted Date: October 20th, 2026

DOI: https://doi.org/10.21203/rs.3.rs-11433017/v1

License: This work is licensed under a Creative Commons Attribution 4.0 International License. Read Full License

Additional Declarations: The authors declare no competing interests.

Collision-Aware Coordination of Dual Drilling Manipulators Using RoboCompiler and Control Barrier Functions

Mehdi Heydari Shahna[a,*], Tuomo Kivelä[b], Jouni Mattila[a]

[a] *Faculty of Engineering and Natural Sciences, Tampere University, 33720 Tampere, Finland.*
[b] *Sandvik Mining and Construction Oy, Tampere, Finland.*

Abstract

Concurrent drilling with two hydraulic booms requires coordinated motion in a confined workspace under actuator limits and intentional tool–rock contact. This paper couples RoboCompiler mechanism models with a centralized control barrier function quadratic program. Independently compiled graphs provide closed-chain kinematics, actuator maps, and reduced dynamics. The program selects actuator commands and reference-progress rates under collision, nominal effort, and flow constraints, reserving clearance for delay, hydraulic response, uncertainty, and stopping travel; a supervisor sequences routing, guarded contact, drilling, and recovery. A twelve-hole MuJoCo mission completed 48.035 m of modeled drilling; in comparison missions, concurrent operation was 42.5% shorter than sequential operation. A 100-collar docking campaign completed 294 of 300 operations across three conditions with no monitored clearance violation and pre-contact feed-extension rates below 20 mm/s; five single-condition ablations assess routing, online filtering, and uncertainty allowances. Isaac Sim checks confirm exported geometry, tree dynamics, and closed-chain static equilibrium.

Keywords: drilling-boom automation; dual-manipulator coordination; control barrier functions; hydraulic manipulators; collision avoidance; underground construction

*Corresponding author: Mehdi Heydari Shahna
E-mail address: mehdi.heydarishahna@tuni.fi

1. Introduction

Automating the manipulators of construction and mining machines can improve the repeatability of tool positioning and reduce the need for operators to remain close to active work areas [1, 2, 3]. Underground drilling is a demanding case: several long-reach hydraulic booms on one carrier must reach a prescribed hole pattern within a shared, confined workspace. Productive operation requires the booms to move concurrently, position their tools accurately, and establish supported contact with the rock before drilling. Earlier work in construction-oriented drilling includes an automated machine concept for tunnelling and underground mining [4] and a rocky-wall consolidation system integrating a drilling rig, a rod-handling manipulator, and automatic rod feeding and recovery [5].

Collision avoidance, task coordination, and hydraulic actuation are coupled throughout such a sequence. A boom moving to its next target can obstruct one that is aligning, drilling, or retracting, and its occupied volume depends on the whole mechanism, including cylinders, closed linkages, and telescopic feed stages. A changed command does not take effect immediately: hydraulic response, command delay, and residual plant motion affect both tracking and stopping, so the required clearance must cover the motion that continues during braking [6, 7]. In addition, tool–rock contact is intentional, whereas all other contact remains prohibited. Contact loads also affect drilling performance. In experiments on robotic concrete drilling, Ortner and Kromoser [8] found that higher feed rates reduced drilling time, although the reduction was not proportional to the increase in drilling forces. This related application motivates considering process loads alongside motion coordination.

Prior work on drilling-boom automation has addressed motion planning and collision avoidance. Kivelä et al. [1] combined coordinate control with online reference modification and potential-field-based avoidance, including simultaneous operation of two drilling booms in simulation. Cui et al. [2] addressed a three-arm tunnel drilling robot through hole sequencing, improved potential-field planning, and trajectory smoothing, supported by physical-machine experiments. Xu and Lin [9] combined kinematic error compensation with a sampling-based planner; their planning study moved the middle boom while representing the outer booms as obstacles. These methods select tool targets and generate admissible geometric routes. Coordinated execution also requires both moving booms to be adjusted online when actuator response, available capacity, or contact conditions change along those routes.

For a single drilling boom, pose-parameterized motion planning and measured-state inverse kinematics were combined with self-collision filtering in [10], where control barrier functions (CBFs) constrain joint velocities through a quadratic program (QP) that modifies the nominal positioning command when a self-collision constraint becomes active. Extending this approach to concurrent drilling requires mutual constraints involving both mechanisms, environmental clearance, and coordinated decisions on how quickly each reference advances. For hydraulic booms, these decisions must also reflect the relation between commanded actuator motion, delivered motion, and the distance needed to stop.

Multi-manipulator safety control offers related formulations. Kaypak et al. [11] developed centralized and decentralized high-order CBF formulations for multiple robotic arms, using convex collision geometry together with joint, velocity, and torque bounds, and reported simulation and hardware studies. Wei et al. [12] used differentiable optimization to construct collision constraints for convex primitives and demonstrated torque-level control in manipulation and contact tasks. Palmieri et al. [13] combined hierarchical QP control, CBF constraints, inter-arm avoidance, and admittance in a semi-autonomous agricultural robot, with laboratory and vineyard experiments. Applying these formulations to drilling machinery additionally requires the transmission geometry and response of hydraulic closed-chain mechanisms to enter the coordination problem.

For hydraulic machines, Shen and Sloth [3] incorporated disturbance estimation and input-delay compensation into robust CBF control of an industrial wheel loader. Huang et al. [14] combined kinematic CBF constraints on excavator joint velocities with a disturbance-observer-based adaptive sliding-mode tracking controller, evaluated in simulation. Backup CBF methods provide constructions for preserving safety under bounded inputs by relating admissible states to a specified backup controller [15]. For mechanism modeling, URDF+ [16] and Extended URDF [17] represent closed-chain and coupled mechanisms, and RoboCompiler [18] compiles a mechanism graph into closure equations, motion maps, actuator-transmission maps, and reduced dynamics, so that geometry and effort are evaluated from one mechanical description.

The problem addressed here is the integration of these capabilities for concurrent drilling: geometric constraints evaluated through the closed-chain motion maps, hydraulic limits expressed in the coordinates of the commanded actuators, clearance that covers delayed response and stopping travel, and regulation of both tasks across free motion and pressure-mode drilling. Table 1

relates this integration to representative prior work.

Table 1 Scope of representative prior work and the capabilities integrated in the proposed framework.

Study or direction	Established capability	Integration in the proposed framework
Kivelä et al. [1]	Online collision-aware references and simultaneous two-boom drilling in simulation.	Centralized command and progress regulation with explicit hydraulic response, capacity, and stopping constraints.
Drilling planners [2, 9]	Multi-arm task and path planning, geometric collision avoidance, and positioning refinement.	Measured-state safety filtering during concurrent motion and transitions between positioning and drilling.
Single-boom CBF [10]	Pose-based planning and joint-velocity self-collision filtering.	Compiled actuator coordinates, mutual and environmental clearance, and coupled reference progress.
Kaypak et al. [11]	Multi-arm CBF coordination with joint, velocity, and torque bounds.	Hydraulic closed-chain mechanisms, pending commands, and reserves for bounded stopping travel.
Interaction control [12, 13]	Constrained manipulation, contact tasks, and supervisory mode switching.	Guarded drilling contact, support-force checks, pressure-mode flow caps, and feed-sweep clearance.
Hydraulic-machine safety [3, 14]	Disturbance- and delay-aware CBF control on a wheel loader; excavator kinematic CBF control with disturbance-observer-based tracking.	Coupled two-boom geometry and residual-motion allowances during backup stopping.
RoboCompiler [18]	Consistent closed-chain motion, actuation, and reduced-dynamics interfaces.	Connection of independently compiled mechanisms to hydraulic safety filtering and drilling supervision.

This paper presents a coordination framework for two mirrored hydraulic drilling booms on a common carrier. RoboCompiler compiles the physical graph of each boom independently and supplies closed-configuration reconstruction, tool and body Jacobians, actuator-effort maps, and reduced dynamics in actuator coordinates, so that the collision model and the tool controller share one mechanism description. A centralized QP selects the commands of the eighteen actuator channels, which are rate references in rate-controlled modes and admissible flow caps in pressure-control modes, together with a reference-progress rate for each boom; either boom can therefore slow, pause, or yield when clearance or hydraulic capacity becomes restrictive. The constraints cover self-, inter-boom, and environmental clearance, actuator limits, nominal hydraulic effort, and the flow budget of each boom. Each clearance constraint reserves distance for estimation and geometry uncertainty,

command delay, hydraulic lag, slew-limited braking, and residual plant motion, and a backup-compatible barrier condition keeps a prescribed slew-limited stop admissible. A supervisor sequences routing, yielding, guarded approach, support engagement, pressure-mode drilling, and retreat or recovery, and sets the permitted contacts and actuator modes of each phase.

The main contributions are:

1. A centralized formulation that regulates the actuator commands and reference progress of two independently compiled closed-chain hydraulic booms. Tool tracking, the clearance constraints (mutual, self-, and environmental), and the nominal effort and flow limits are all expressed in common actuator coordinates.
2. A stopping-aware barrier construction that combines pending-command prediction, hydraulic response, slew-limited braking, residual-motion memory, and uncertainty allowances in affine QP constraints, and states the conditions under which a specified backup stop preserves clearance across controller updates.
3. Contact supervision that coordinates guarded approach, pressure-mode drilling, feed-sweep clearance, and recovery with motion, evaluated in simulation through a twelve-hole drilling mission with controller comparisons, a 100-collar docking campaign (three conditions for the full framework and five ablations under one condition), and Isaac Sim checks of the exported model.

2. Application of RoboCompiler to two drilling mechanisms

RoboCompiler [18] supplies the mechanical interfaces of each boom to a centralized, actuator-aware CBF filter (Fig. 1). The previous single-boom method combined measured-state inverse kinematics with joint-velocity self-collision filtering [10]; the present filter works in actuator coordinates and incorporates hydraulic response, command delay, stopping travel, nominal force/flow constraints, and mutual, self-, and environmental clearance.

Each boom has a graph $\mathcal{G}_b = (\mathcal{V}_b, \mathcal{E}_b, \mathcal{A}_b)$, $b \in \{L, R\}$, containing rigid bodies and inertias, joints and attachment frames, and actuator ports. Cylinder bodies and rods close the shoulder and wrist linkages. Telescopic stages satisfy $d_{bj} = k_j d_{b1} + o_j$, with master stroke d_{b1}, gain k_j, and offset o_j.

The right boom reflects the left graph while retaining separate states,

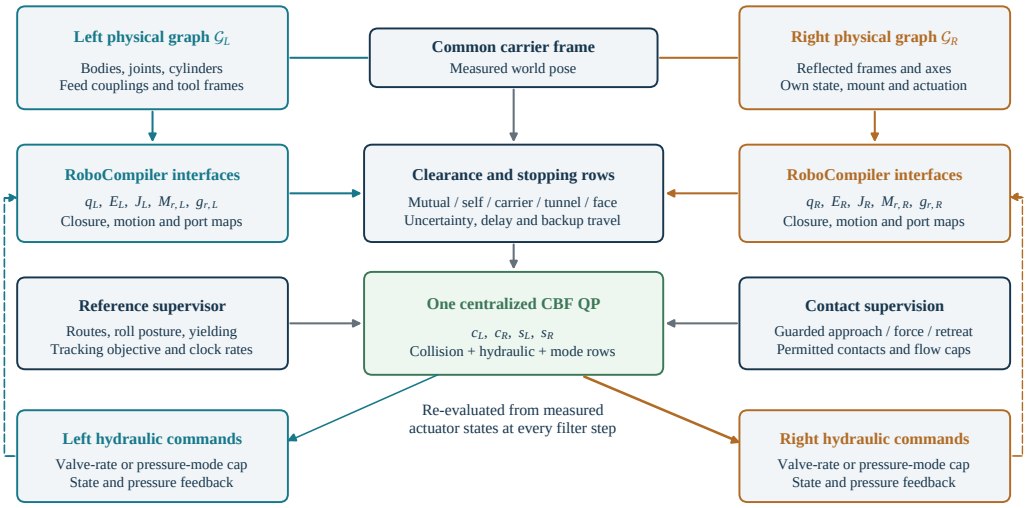

Fig. 1. Coordination architecture. Each physical graph supplies closure, geometry, and dynamics interfaces. A centralized filter selects both actuator commands and reference-progress rates using shared clearance constraints and contact-dependent supervision.

mounts, and commands. With $S = \mathrm{diag}(1, -1, 1)$ and $\bar{S} = \mathrm{diag}(S, 1)$,

$$\begin{aligned} T^R &= \bar{S} T^L \bar{S}, \qquad r^R = S r^L, \qquad \mathcal{I}^R = S \mathcal{I}^L S^\mathsf{T}, \\ a^R_{\mathrm{rev}} &= -S a^L_{\mathrm{rev}}, \quad a^R_{\mathrm{pris}} = S a^L_{\mathrm{pris}}, \end{aligned} \tag{1}$$

where T is a joint or named-frame transform, r the center of mass, $\mathcal{I}$ its inertia, and a a joint axis. Conjugation preserves right-handed frames, and the revolute-axis sign preserves axial-vector transformation. Reflection retains connectivity, closure, and actuator conventions. Each graph is compiled independently; centralized coordination adds a second nine-coordinate command block and inter-boom clearance rows. Figure 2 shows the five independent cycles and two feed-coordinate couplings of each instance.

2.1. Closed-chain configuration and motion interfaces

The actuator vector $x_b \in \mathbb{R}^9$ comprises swing, lift, zoom, tilt, feed-swing, roll, bolting, feed-extension, and master-feed coordinates; all are lengths except roll. Rod spin φ_b is a separate process coordinate with axisymmetric collision geometry. For augmented configuration q_b and $u_b = (x_b^\mathsf{T}, \varphi_b)^\mathsf{T}$,

$$\Phi_b(q_b) = 0, \qquad q_b = \mathcal{Q}_b(u_b), \qquad \dot{q}_b = N_b(q_b)\dot{u}_b, \tag{2}$$

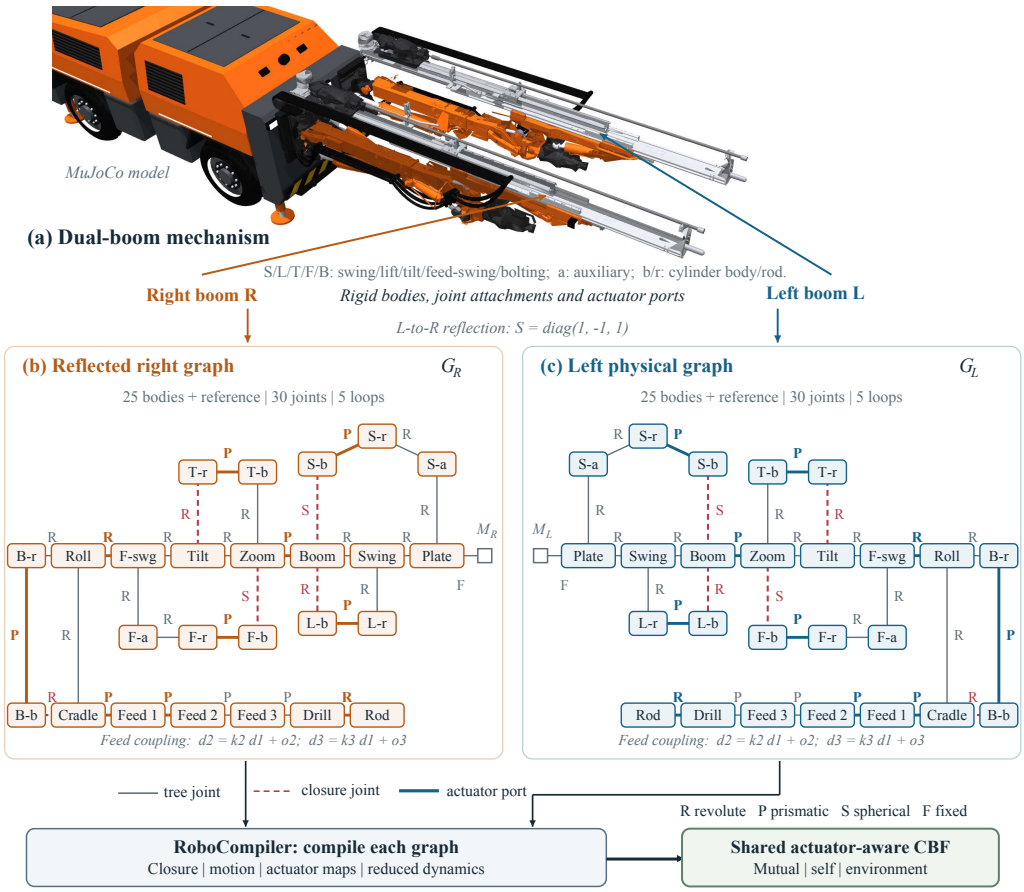

Fig. 2. Dual-boom mechanism and physical graphs. (a) Carrier-mounted mechanisms in MuJoCo. (b,c) Reflected right and left graphs: rounded vertices denote rigid bodies, squares mounting references M_b, solid/dashed edges tree/closure joints, and thick colored edges actuator ports. Each graph has 25 bodies, 30 joints, and five independent cycles; feed couplings are coordinate relations. Separately compiled interfaces enter the centralized CBF filter.

where Φ_b contains loop residuals and $N_b = D\mathcal{Q}_b$ satisfies $D\Phi_b N_b = 0$. Its nine x_b columns form E_b. Continuation and closure correction reconstruct dependent coordinates from measured actuator coordinates, subject to the full residual tolerance, the selected assembly branch, and a regular dependent-coordinate Jacobian.

Body j is located in world frame W through carrier frame K and mount M_b:

$$ {}^{W}T_{bj} = {}^{W}T_{K}\,{}^{K}T_{M_b}\,\widetilde{T}_{bj}(\mathcal{Q}_b(u_b), \hat{\theta}_b). \tag{3} $$

Here ${}^{W}T_K$ is the measured carrier pose and $\hat{\theta}_b \in \mathbb{R}^3$ an estimated three-axis orientation correction. The corrected pose $\widetilde{T}_{bj}$ applies this rotation to distal bodies about a specified reference node while preserving proximal poses. Actuator Jacobians hold the carrier pose and orientation correction fixed within each control step; geometric error allowances and residual-response terms cover their unresolved motion.

For body-fixed point p, $\dot{p} = J_{p,b}\dot{x}_b$ and $\omega = J_{\omega,b}\dot{x}_b$; hence the drilling axis satisfies $\dot{a}_b = \omega \times a_b$. Tool regulation and the clearance constraints use these same Jacobians.

2.2. Reduced dynamics and contact-load interfaces

With rod spin fixed, $E_{T,b}$ restricts E_b to physical-tree velocities. The actuator map L_b and contact Jacobian $J_{c,b}$ preserve power:

$$\dot{\ell}_b = L_b\dot{x}_b, \quad \tau_{a,b} = L_b^{\mathsf{T}} f_b, \quad \tau_{c,b} = J_{c,b}^{\mathsf{T}} w_b. \tag{4}$$

Here ℓ_b is actuator displacement, f_b transmitted force or torque, w_b stacked external forces or wrenches, and $\tau_{a,b}, \tau_{c,b}$ their reduced efforts. The chosen coordinates give $L_b = I$. Eliminating internal loop reactions from tree inertia $M_{T,b}$ and bias $h_{T,b}$ [19] yields

$$\begin{aligned} &M_{r,b} = E_{T,b}^{\mathsf{T}} M_{T,b} E_{T,b}, \quad h_{r,b} = E_{T,b}^{\mathsf{T}}(h_{T,b} + M_{T,b}\dot{E}_{T,b}\dot{x}_b), \\ &M_{r,b}\ddot{x}_b + h_{r,b} = L_b^{\mathsf{T}} f_b + J_{c,b}^{\mathsf{T}} w_b. \end{aligned} \tag{5}$$

The derivative $\dot{E}_{T,b}$ follows the closed configuration path; auxiliary closure-chart coordinates are massless.

For positioning, the filter uses inertia frozen at the latest model update and gravity bias $g_{r,b} = h_{r,b}(x_b, 0)$. The orientation correction used in Eq. (3) is supplied by a prescribed load-dependent geometry map:

$$\hat{\theta}_b = \Psi_b(x_b, w_b). \tag{6}$$

For the measured carrier pose, Ψ_b returns the three-axis correction from actuator configuration and external loading, including gravity. The coordination filter uses this correction and its stated error bounds as inputs. Residual body motion, cross-boom coupling, and carrier response enter the stopping-response budget.

3. Hydraulic actuation and command feasibility

Each boom has a separate hydraulic supply governed by chamber continuity, friction, and compensated metering [20] (Appendix A). The filter selects actuator-rate commands c_b using the identified response

$$v_b^{\text{next}} = (I - K_b)v_b + K_b c_b, \qquad K_b = \text{diag}(1 - e^{-\Delta t/\tau_{bj}}), \tag{7}$$

where $v_b = \dot{x}_b$, τ_{bj} is effective response time, and Δt the control period. Before spool conversion, pressure feedback gives $\tilde{c}_j = c_j - F_{\text{hp},j}/B_{v,j}$, with high-pass chamber effort $F_{\text{hp},j}$ and $B_{v,j} = 2\zeta_j\sqrt{k_{h,j}M_{r,jj}}$. Here ζ_j is damping ratio and $k_{h,j} = \beta_e(D_{A,j}^2/V_{A,j} + D_{B,j}^2/V_{B,j})$ oil stiffness, defined by bulk modulus β_e, effective areas $D_{A,j}, D_{B,j}$, and chamber volumes $V_{A,j}, V_{B,j}$. The identified response and its reserve include this inner feedback.

Phase restrictions, speed limits, and slew bounds $|c_{bj} - c_{bj}^-| \leq a_{bj}\Delta t$ constrain commands, with pending command c_{bj}^- and rate-of-change bound a_{bj}. Extension capacity is

$$p_{A,\text{req}} = \frac{g_{r,j} + F_{C,j} + D_{B,j}(p_T + p_c)}{D_{A,j}}, \quad \bar{c}_j^+ = \eta_v \frac{Q_{\text{nom},j}}{D_{A,j}}\phi(p_{\text{in,max},j} - p_{A,\text{req}}), \tag{8}$$

where $F_{C,j}$ is Coulomb friction, p_T tank pressure, p_c compensator drop, $Q_{\text{nom},j}$ full-opening flow, and ϕ the metering function in Eq. (A.2). The inlet limit $p_{\text{in,max},j}$ is the smaller pump/port limit, and η_v reserves valve capacity. Retraction exchanges chamber areas and reverses the load sign. The nominal supply budget is

$$\sum_j q_{bj} \leq Q_{\text{avail},b}, \quad q_{bj} \geq D_{A,j}c_{bj},\ -D_{B,j}c_{bj},\ 0, \tag{9}$$

where q_{bj} is a flow epigraph and $Q_{\text{avail},b} = \max(\eta_Q Q_{\text{max},b} - Q_{\text{perc},b} - Q_{\text{res},b}, 0)$. Pump capacity $Q_{\text{max},b}$ is reduced by reserve factor $\eta_Q \in (0, 1]$, percussion flow $Q_{\text{perc},b}$, and reserved branch flow $Q_{\text{res},b}$.

4. Collision geometry and stopping-aware barriers

4.1. Coverage of the two booms and the environment

The shared constraints cover mutual and self-collision, carrier obstacles, tunnel boundaries, the rock face, and actuator/joint limits (Fig. 3). Graph-frame convex pieces provide closest-point distances [21]; enclosing capsules

provide broad-phase lower bounds. Pruning requires these bounds to exceed the clearance allowance and reachable stopping envelope.

For witnesses p_A, p_B and normal n directed from A to B,

$$\dot{d}_i = g_i \dot{x}, \qquad g_i = n^{\mathsf{T}}(J_B - J_A), \quad x = (x_L^{\mathsf{T}}, x_R^{\mathsf{T}})^{\mathsf{T}}. \tag{10}$$

The Jacobians contain both booms' columns and zero columns for fixed obstacles. Mutual rows thus couple commands while retaining separate physical graphs. Witness gradients apply locally; point-speed bounds accommodate witness changes during braking. For capsule endpoints p_0, p_1, radius r, and angular Jacobian column $J_{\omega,j}$,

$$\pi_j = \max(\|J_{p_0,j}\|, \|J_{p_1,j}\|) + r\|J_{\omega,j}\|. \tag{11}$$

Self-collision bounds remove common rigid-body motion through relative twists. Nonnegative P_{ij}, Q_{ij} bound clearance-loss rates for positive and negative actuator motion. Symmetric geometric bounds give $P_{ij} = Q_{ij}$; scalar limits use $P_{ij} = \max(-g_{ij}, 0)$ and $Q_{ij} = \max(g_{ij}, 0)$.

For rock-face height $X_f(Y, Z)$, smooth lower surface $X_c \leq X_f$, and slope bound L_f, free-side clearance satisfies

$$\underline{d}_f(p) = \frac{X_c(p_Y, p_Z) - p_X}{\sqrt{1 + L_f^2}}. \tag{12}$$

Subtracting probe radii and capsule-axis half-spacing covers the represented surface between samples. Tunnel rows use hull vertices and analytic boundary distances. Multiple samples use the conservative soft minimum $d_i = -\kappa_d^{-1} \log \sum_\ell e^{-\kappa_d d_{i\ell}}$, $\kappa_d > 0$.

Explicit exclusions cover joint neighbors, guided feed stages, and rigid attachments. Further exclusions use branch-and-bound mesh-clearance searches over joint limits, conditional on grid-estimated speed constants bounding the continuum. Policy clearances apply to actively constrained pairs.

4.2. Uncertainty reserve and stopping distance

Each geometric row requires $D_i = d_i^{\text{pol}} + m_i$, where d_i^{pol} is the policy clearance and

$$m_i = \sum_j |g_{ij}|\epsilon_{x,j} + (\ell_{iL} + \ell_{iR})\epsilon_\theta + \chi_i^W(\epsilon_{Kt} + \ell_{iK}\epsilon_{Kr}) + \rho_i + h_{\text{fb}}. \tag{13}$$

Here $\epsilon_{x,j}$ bounds the actuator-coordinate error. The scalars ϵ_θ and $(\epsilon_{Kt}, \epsilon_{Kr})$ bound the Euclidean norms of the orientation-correction error and of the

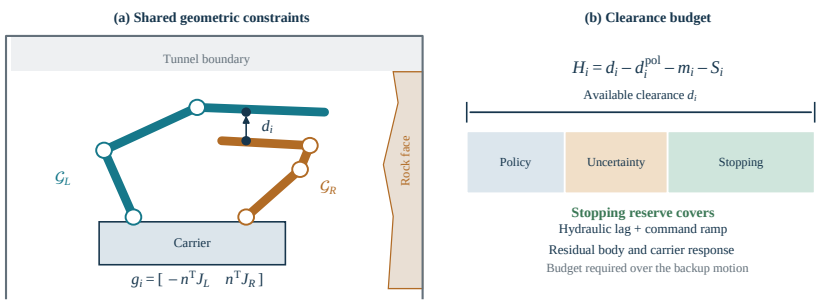

Fig. 3. Shared collision constraints. Mutual-clearance rows couple both booms; environment and self-collision rows enter the same optimization. Clearance covers policy separation, uncertainty, and backup motion, using local witness gradients and bounded point speeds.

carrier translation and rotation errors. Each equals the norm of the corresponding per-axis bounds, so an orientation error displaces a point at lever ℓ by at most $\ell\epsilon_\theta$, to first order. Levers ℓ_{ib}, ℓ_{iK} bound distances from the correction reference nodes and the carrier rotation center; χ_i^W selects world-obstacle rows. Common carrier-pose errors cancel in mutual distances. The reserve ρ_i covers geometry, interpolation, and one-step linearization; $h_{\mathrm{fb}} > 0$ sets the recovery band. Rate-response uncertainty enters the stopping reserve. Joint/stroke rows use pre-shrunk limits in their coordinate units.

The backup ramps each rate-controlled actuator toward zero and closes its valve at zero command:

$$c_j^{\mathrm{br}} = c_j^- - \mathrm{sgn}(c_j^-)\min(|c_j^-|, a_j\Delta t). \tag{14}$$

Define $c_j^+ = \max(c_j, 0)$, $c_j^{\ominus} = \max(-c_j, 0)$, $\nu_j^+ = \max(v_j, c_j, 0)$, and $\nu_j^- = \max(-v_j, -c_j, 0)$. A convex piecewise-linear ramp majorant satisfies $\mathcal{R}_j(z) \geq z^2/(2a_j)$ and $\mathcal{R}_j'(z) \geq z/a_j$ throughout the rate domain. The shared stopping reserve and barrier are

$$\begin{aligned} S_i = &\sum_j T_j(P_{ij}\nu_j^+ + Q_{ij}\nu_j^-) + \sum_j \left[P_{ij}\mathcal{R}_j(c_j^+) + Q_{ij}\mathcal{R}_j(c_j^{\ominus})\right] \\ &+ \sum_j A_{ij}(|c_j| + z_j^r) + \sum_j B_{ij} z_j^s, \quad H_i = d_i - D_i - S_i. \end{aligned} \tag{15}$$

Effective lag times T_j, ramp bounds, and residual-response gains A_{ij}, B_{ij} include response inflation $\iota \geq 1$. The additional terms bound residual body motion, cross-boom coupling, and carrier motion following command changes.

Nonnegative slew and step memories evolve as

$$\begin{aligned} z_j^{r,+} &= \lambda_j z_j^r + \min(|\Delta c_j|, a_j \Delta t), \\ z_j^{s,+} &= \lambda_j z_j^s + \max(|\Delta c_j| - a_j \Delta t, 0), \end{aligned} \tag{16}$$

where Δc_j is the applied command change and $\lambda_j = e^{-\Delta t/\tau_{\mathrm{ring},j}}$ follows residual-response decay time $\tau_{\mathrm{ring},j}$. Slew-limited commands excite z^r; excess steps also excite z^s.

The condition $H_i \geq 0$ ensures separation throughout a backup continued to rest, provided the estimation allowance and response, clearance-speed, and residual-motion bounds hold throughout that physically realizable stop. This interpretation uses the assumed contact modes, control period, and zero rates for hydraulically locked actuators. Rate uncertainty is represented through response inflation. Forced backup stops (Section 7.1, Appendix D) test these assumptions against realized stopping travel, actuator motion, and clearance.

5. Centralized online CBF coordination

5.1. Delayed prediction and barrier constraints

A centralized quadratic program separates tracking from admissibility [22, 23], accounting for actuator response and one-cycle command latency [24]. Stack $v = (v_L^\mathsf{T}, v_R^\mathsf{T})^\mathsf{T}$, $c = (c_L^\mathsf{T}, c_R^\mathsf{T})^\mathsf{T}$ and $K = \mathrm{blkdiag}(K_L, K_R)$. Estimated state (x, v) and pending command c^- give

$$\begin{aligned} v^{(1)} &= (I-K)v + Kc^-, & \Delta x^{(1)} &= \tfrac{\Delta t}{2}(v + v^{(1)}), \\ v^{(2)}(c) &= (I-K)v^{(1)} + Kc, & \Delta x^{(2)}(c) &= \tfrac{\Delta t}{2}(v^{(1)} + v^{(2)}(c)). \end{aligned} \tag{17}$$

The first interval is committed. Define $e_i^{(1)} = d_i - D_i + g_i \Delta x^{(1)}$ and $e_i^{(2)}(c) = e_i^{(1)} + g_i \Delta x^{(2)}(c)$. A nonnegative pressure-mode flow cap uses $\min(g_{ij}, 0)$ for command-dependent clearance and is treated as instantaneously closable. Slew/ramp terms apply to rate-mode columns, which retain g_{ij}; valves closed beyond their stopping time use zero rate under hydraulic locking, with clearances updated from measured positions. Equation (15) gives predicted barriers $\widehat{H}_i^{(1)}$ and $\widehat{H}_i^{(2)}(c)$. The hard collision row is

$$\widehat{H}_i^{(2)}(c) \geq t_i, \qquad t_i = \min\Big\{(1-\gamma\Delta t)\widehat{H}_i^{(1)}, \widehat{H}_i^{(2)}(c^{\mathrm{br}})\Big\}, \tag{18}$$

where $\gamma > 0$ and $0 < \gamma\Delta t \leq 1$. The minimum admits the backup. For frozen prediction data, $T_j \geq \Delta t(1/K_{jj} - 1/2)$ and the ramp-slope condition yield

$\widehat{H}_i^{(2)}(c^{\mathrm{br}}) \geq \widehat{H}_i^{(1)}$. Appendix C relates this property to measured inter-cycle prediction defects and mode transitions.

Linear epigraphs represent maxima, absolute values, and ramp majorants: $w_j^+ \geq v_j^{(2)}, c_j, 0$, $w_j^- \geq -v_j^{(2)}, -c_j, 0$, and $y_j^\pm \geq m_{j\ell}(\pm c_j) + b_{j\ell}$ for ramp-segment slopes $m_{j\ell}$ and intercepts $b_{j\ell}$. Collision rows are affine and hard in the expanded decision vector.

Within the geometric recovery band $-h_{\mathrm{fb}} \leq e_i^{(1)} < 0$, the target becomes

$$t_i \leftarrow \min\{t_i, e_i^{(1)} - \eta_b(h_{\mathrm{fb}} + e_i^{(1)})\}, \tag{19}$$

where $\eta_b \in (0,1)$. The additional condition $g_i \Delta x^{(2)}(c) \geq \min\{0, g_i \Delta x^{(2)}(c^{\mathrm{br}})\}$ limits predicted clearance loss to the backup's. The stopping guard is

$$\widehat{H}_i^{\mathrm{guard}} = e_i^{(1)} - S_i^{(1)}/\iota, \tag{20}$$

with inflated committed-state reserve $S_i^{(1)}$. A geometric guard below $-h_{\mathrm{fb}}$ or solver failure applies Eq. (14) to both booms and freezes reference progress.

5.2. Tracking objective and hydraulic effort rows

Each boom's reference clock advances at $\dot{\vartheta}_b = s_b \in [0,1]$. Transit and terminal-alignment maps define J_b, feedforward $w_{\mathrm{ff},b}$, and feedback $w_{\mathrm{fb},b}$ (Appendix C). Commands (c_L, c_R), progress rates (s_L, s_R), and epigraph variables minimize

$$\sum_b \Big(\|J_b c_b - s_b w_{\mathrm{ff},b} - w_{\mathrm{fb},b}\|_{Q_b}^2 + \rho_b (1 - s_b)^2 + \|c_b - c_b^{\mathrm{pref}}\|_{\Lambda_b}^2 \Big), \tag{21}$$

subject to Eqs. (9), (18), and (22), command/limit bounds, and contact-mode rows. Here c_b^{pref} is a secondary rate preference and $\|z\|_Q^2 = z^\mathsf{T} Q z$, with $Q_b, \Lambda_b \succeq 0$ and $\rho_b \geq 0$. The positioning block of Λ_b uses reduced inertia normalized by a nominal-speed energy scale, providing a physical metric across linear/angular coordinates. Small regularization makes the expanded Hessian positive definite.

Let diagonal R_b have entry one in rate mode and zero in pressure-cap mode, $K_{v,b} = K_b R_b$, and $\bar{v}_b^{(2)} = (I - K_{v,b}) v_b^{(1)} + K_{v,b} c_b$. Nominal acceleration and braking-effort constraints are

$$\begin{aligned} F_b^- &\leq M_{r,b} \frac{K_{v,b}(c_b - v_b^{(1)})}{\Delta t} + g_{r,b} + f_{\mathrm{fr},b}(v_b^{(1)}) \leq F_b^+, \\ F_b^- &\leq -M_{r,b} \frac{K_b \bar{v}_b^{(2)}}{\Delta t} + g_{r,b} \leq F_b^+, \end{aligned} \tag{22}$$

where $F_j^+ = D_{A,j}p_{\mathrm{rel},j} - D_{B,j}p_T$ and $F_j^- = -(D_{B,j}p_{\mathrm{rel},j} - D_{A,j}p_T)$ bound hydraulic effort f_j^{h} at port-relief pressure $p_{\mathrm{rel},j}$. The first row includes friction and prescribes acceleration only in rate mode. The second estimates gravity-loaded abrupt decay; the applied backup remains slew-limited.

These rigid-model estimates are compared with chamber efforts in free motion, valve closure, and loaded operation in Appendix D; Appendix C specifies the discrepancy bound required for robust tightening, and the reported nominal missions use the untightened limits. When the nominal force/flow limits would exclude c^{br}, they are widened to admit it and the excess is recorded; this preserves feasibility of the optimization, whereas physical feasibility depends on the actual actuator and pump capacity. Because the mutual rows contain the commands of both booms and each boom has its own progress rate, either boom can yield temporarily during concurrent operation.

6. Permitted contact and supervisory coordination

Docking and loaded operation use guarded approach and force supervision for designated stinger, bit and rod contacts. Outside these phases, the same bodies obey rock-face avoidance. Other feed bodies retain front-face clearance, and mutual-boom, carrier, self-collision and tunnel constraints remain active throughout.

For estimated axial face gap g_c, gap-error allowance δ_c and approach-speed limit $\bar{v}_c$, the guarded contact row is

$$H_c = \max(g_c - \delta_c, 0) + T_c\bar{v}_c - S_c \geq 0. \tag{23}$$

Here S_c is one-sided stopping travel and T_c the minimum effective lag among closing actuators. Equation (18) enforces the next-state row until force establishes support. The positive part is evaluated at the measured state before the program is assembled: the row enters with the constant $\max(g_c - \delta_c, 0)$ and with the gap Jacobian multiplied by σ_c, where $\sigma_c = 1$ if $g_c > \delta_c$ and $\sigma_c = 0$ otherwise, so it is affine in the decision variables. Since $\max(z, 0) \geq z$ and $\max(z, 0) \geq 0$, this expression never exceeds the clipped first-order prediction, and the affine row is a restriction of the clipped one. The stopping travel S_c always uses the unclipped gap Jacobian; for $g_c \leq \delta_c$ the row therefore limits only the closing rate. The gap Jacobian follows from $F(p + g_c a) = 0$, with $F(p) = X_f(p_Y, p_Z) - p_X$. Sensing, carrier-pose, face-interpolation and orientation-correction errors are amplified by $\|\nabla F\|/|\nabla F^{\mathsf{T}} a|$; admissible

approaches require a finite gap-error bound. Search-distance and time limits terminate unsuccessful attempts.

After the feed extension establishes support at F^*_{ext}, the bit advances under a second guarded row and enters pressure mode with thrust

$$F^*_{\text{bit}} \leq \min(F_{\text{nom}}, F_{\text{bit,max}}, F^*_{\text{ext}} - F_{\text{st,min}}), \tag{24}$$

where F_{nom}, $F_{\text{bit,max}}$ and $F_{\text{st,min}}$ are requested thrust, maximum bit force and minimum support force. Thrust is ramped and reduced when support falls below its minimum. For telescopic gain $\kappa_f = \partial z_{\text{bit}}/\partial d_{b1}$, relating axial bit travel to master stroke, pressure targets satisfy

$$\begin{aligned} D_{A,\text{feed}} p^*_{A,\text{feed}} &= \kappa_f F^*_{\text{bit}} + F_{C,\text{feed}} + D_{B,\text{feed}} p_{B,\text{feed}}, \\ D_{A,\text{ext}} p^*_{A,\text{ext}} &= F^*_{\text{ext}} + F_{C,\text{ext}} + D_{B,\text{ext}} p_{B,\text{ext}}. \end{aligned} \tag{25}$$

The QP constrains branch flow caps, with separate force-window supervision. Established support replaces the corresponding valve-travel term by $d_c \max(P_{ij}, Q_{ij})$, where d_c bounds residual, uncommanded settling travel of the supported actuator after support establishment.

Before forward feeding, each convex body $\mathcal{B}$ is enlarged to its continuous swept set

$$\mathcal{W} = \mathcal{B} \oplus [0, \ell]a = \text{conv}\,(\mathcal{B} \cup (\mathcal{B} + \ell a)), \tag{26}$$

where ℓ is remaining translation, including feed-stage gains, and $\oplus$ denotes the Minkowski sum. The two envelopes are checked against each other, the carrier, tunnel and own mechanisms for a drilling axis fixed within its error reserve. Online constraints use measured feed positions.

Each boom follows the phase sequence in Fig. 4. Front-load limits, persistent support loss and excessive feed-extension change terminate loaded operation. Extension stroke monitors axial slip; transverse stinger motion is evaluated separately. The supervisor selects actuator-space routes and roll postures, checks joint look-ahead through the same filter, and introduces yielding or retreat when progress stalls. The scaled task-map minimum singular value screens goals and attenuates terminal feedback. Replanning starts from measured states; unsuccessful recovery holds the booms and reports the command as unreachable.

For the 100-collar campaign in Section 7.2, the look-ahead additionally uses the load-dependent geometry correction and a planning allowance, with route endpoints evaluated at the current non-positioning actuator strokes. The supervisor explores alternative routes after predicted stalls and records

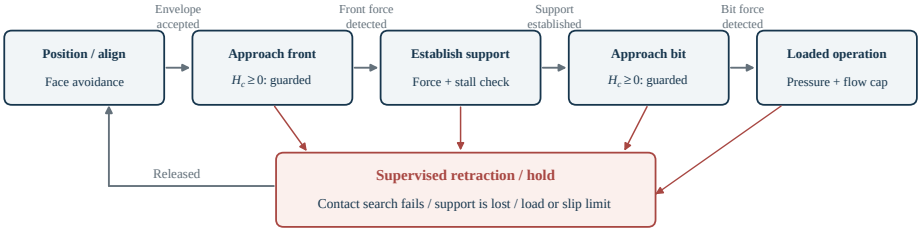

Fig. 4. Per-boom contact supervision within centralized coordination. Approach, force establishment, loaded operation, and retraction select face-contact and actuator modes. Contact failure, excessive load, persistent support loss, or axial slip triggers retreat.

unsuccessful route prefixes to avoid repeating them from nearby states. Recovery returns home and retries the round once, or retraces the recorded motion under the active constraints and proceeds to the next round; persistent planning or recovery failure produces a hold (Appendix F).

The plant couples hydraulic actuation to spatially varying rock strength, percussion-dependent penetration, unilateral bit contact, bore-wall guidance and rotational resistance. Appendix B defines this phenomenological drilling-load model and the separate bore-path drift model.

7. Numerical verification and validation

Timing was measured on two platforms. The demonstration mission and the 100-collar campaign ran on two virtual cores of a cloud server (Intel Xeon, 2.10 GHz) shared by two concurrent missions; the accelerated evaluations ran on a Dell XPS 15 9530 laptop (Intel Core i7-13700H, 32 GB RAM). Appendix D gives the threading and resource conditions.

7.1. Coordinated twelve-hole drilling in a confined tunnel using MuJoCo

Two hydraulic drilling booms on a common carrier completed six paired drilling rounds in MuJoCo [25], referred to below as the demonstration mission: ten face holes and two upward holes, each with a 4.0 m target depth. The mission started and ended at home (Fig. 5). The plant included closed-chain linkages, configuration-dependent body-pose response, four carrier stabilizers with load-dependent support response, hydraulic dynamics, rock interaction, and bounded sensing errors. The plant step was 1 ms; control ran every 10 ms during positioning and contact transitions and every 50 ms in slower phases with closed positioning valves, with a one-period command delay. The plant was stepped synchronously with the controller, so the reported durations are

simulated time and exclude computation. The controller core took 35.7 ms per cycle on average in this mission; in separate accelerated evaluations (twelve-hole missions with 0.3 m holes and round 3 at 4 m), it averaged 5.8–6.1 ms, with about 1% of the 10 ms cycles overrunning. Appendix D gives the target pattern, parameters, and detailed diagnostics.

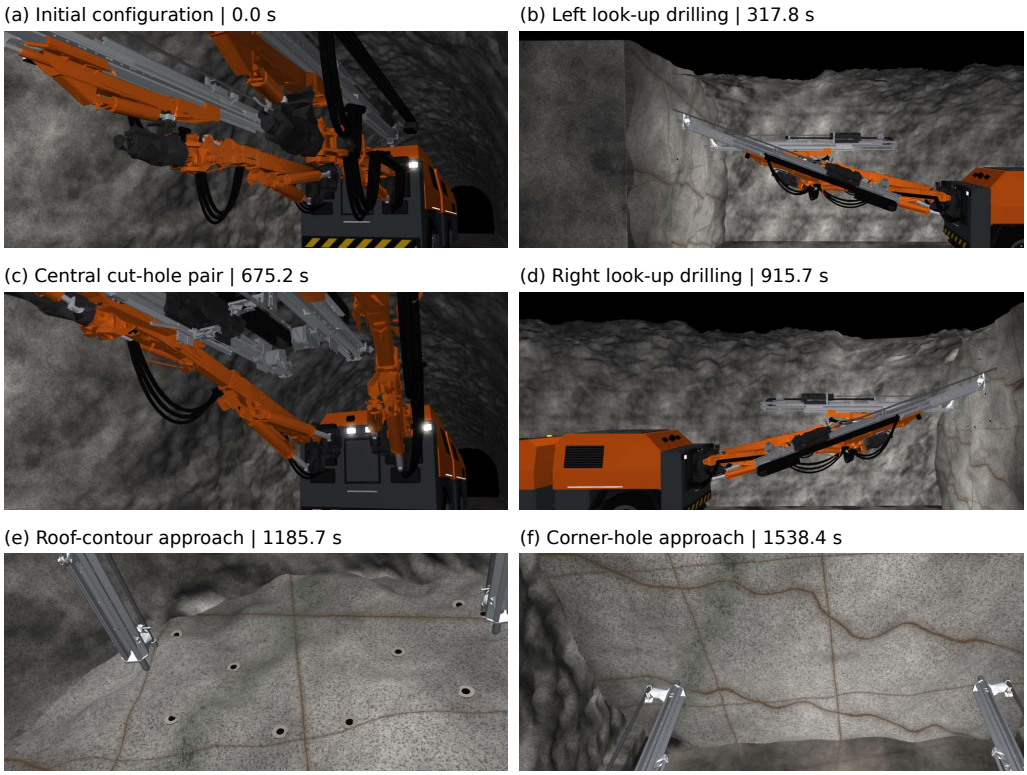

Fig. 5. Representative configurations: (a) home; (b) left upward/right face drilling; (c) central cut holes; (d) right upward/left face drilling; (e) roof-contour approach; and (f) lower-corner approach. Times are elapsed simulation time.

The demonstration mission completed all twelve holes and returned home in 1713.34 s (28.56 min), with 48.035 m of modeled drilling and hole depths of 4.0025–4.0056 m. Both booms drilled concurrently in every round, for 848.99 s in total including anti-jamming intervals (Fig. 6). In round 5, the left boom yielded through home; after a segment timeout at 1168.47 s, replanning completed the repositioning at 1177.27 s. Figure 7 shows the bit-tip paths.

Mean and maximum collar errors were 1.77 and 3.98 mm, and the maximum initial-axis error was 0.0688°. Over 69 668 control cycles, every active

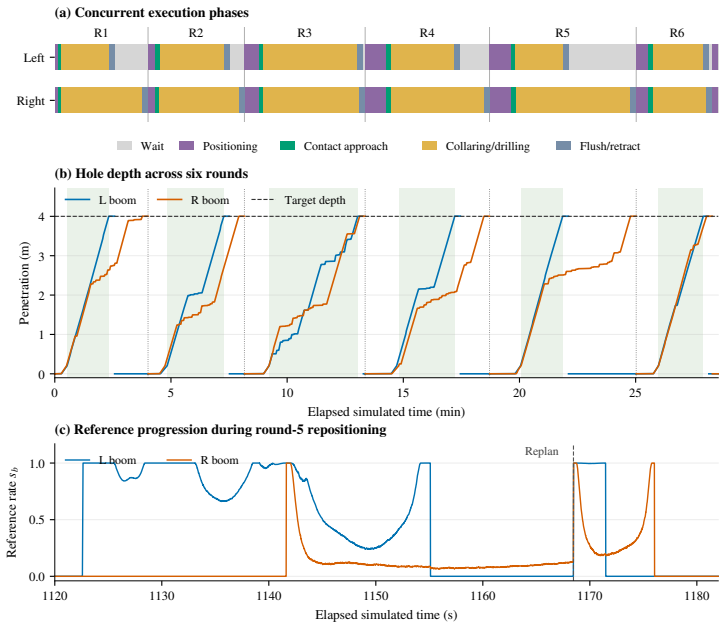

Fig. 6. Six paired rounds: (a) independent phases; (b) hole depths, with concurrent drilling shaded and the 4 m target dashed; and (c) reference-progress rates during round 5, marking the replan at 1168.47 s. Breaks indicate depth-register resets; concurrent drilling includes anti-jamming recovery.

clearance class stayed above its policy; the minimum inter-boom separation was 214.8 mm against a 50 mm policy. No solver failure, guard-triggered fallback, or prohibited contact occurred, and a separate CAD audit found no intersection in 23 730 590 pair checks over 17 134 configurations sampled every 0.1 s. All holes were completed despite 165 anti-jamming activations. The maximum pre-contact feed and axial bit speeds were 11.6 and 9.3 $\mathrm{mm\,s^{-1}}$, below the 20 $\mathrm{mm\,s^{-1}}$ approach limit.

Controller comparisons. Four further missions shared plant parameters, initial conditions, targets, and seeds: the proposed filter in concurrent and in sequential operation; independent actuator-aware filters, each treating the other boom at its measured pose; and a geometric velocity-level CBF with $\gamma = 20\,\mathrm{s}^{-1}$ that keeps the clearance functions, uncertainty allowances, and tracking objectives. Each configuration supplied its own supervisory look-ahead, and independent control planned the booms separately, so the comparison covers complete configurations, including their routes.

All four completed twelve 4 m holes and returned home without prohibited

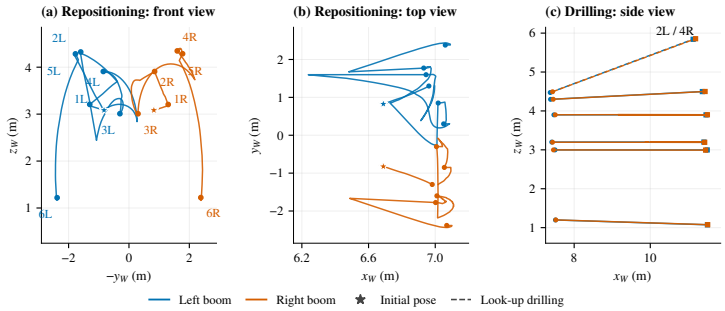

Fig. 7. Plant bit-tip paths sampled at 10 Hz: (a,b) front/top projections of positioning, with round/boom labels at completion and stars at initial poses; (c) collaring/drilling in side view, with upward holes dashed and first/last samples marked by circles/squares. World axes point toward the face (x_W), left (y_W), and upward (z_W).

contact or sampled policy violation (Table 2). Concurrent operation took 1666.57 s, which is 42.5% less than sequential operation (speed-up 1.74); the drilled-length rates were 103.8 and 59.7 m h^{-1}. To remove differences in drilling time, a post hoc schedule replaced the drilling duration of each hole with its value in the proposed concurrent run while keeping the measured non-drilling durations and each scheduling rule (T_{norm}). In this schedule the speed-up over sequential operation was 1.72, the independent filters were 4.97 s faster than the proposed filter, and the geometric CBF was 147.01 s (8.8%) faster. The booms stayed more than 210 mm apart in all four missions, so this target pattern separates the configurations by duration rather than by inter-boom clearance; they differ in clearance when references conflict, as shown next. Each entry is a single execution, and the proposed concurrent run differs from the demonstration mission by 46.77 s.

Table 2 One complete twelve-hole, 4 m mission per controller, each with return home and no sampled policy-clearance violation. T is simulated duration; T_{norm} uses common per-hole drilling durations in a post hoc schedule calculation. Rate is achieved length divided by T; $e_{p,\max}$ and $e_{a,\max}$ are maximum collar/axis errors; $d_{\text{LR},\min}$ is minimum inter-boom clearance.

Controller	T (s)	T_{norm} (s)	Rate (m h^{-1})	$e_{p,\max}$ (mm)	$e_{a,\max}$ (°)	$d_{\text{LR},\min}$ (mm)
Proposed, concurrent	1666.57	1666.57	103.8	3.98	0.0588	211.7
Proposed, sequential	2896.14	2870.76	59.7	4.99	0.0874	227.6
Independent	1723.95	1661.60	100.3	4.09	0.0862	214.7
Geometric CBF ($\gamma = 20$)	1551.57	1519.56	111.5	2.69	0.0489	217.1

Conflicting references and forced stops. With route supervision bypassed, conflicting references drove both booms across the tunnel center. The proposed filter kept 94.47/94.50 mm inter-boom clearance at half/full reference speed and the independent filters 88.85/88.23 mm, against the 50 mm policy. At the same reference speeds, the result of the geometric CBF depended on its gain: $\gamma = 20\,\mathrm{s}^{-1}$ gave minimum separations of $0.88/-0.62$ mm, with contact at full speed, whereas $\gamma = 5\,\mathrm{s}^{-1}$ kept 75.22/77.15 mm. Unlike the geometric CBF, the proposed barrier reserves stopping travel computed from the identified response and braking limits. The proposed filter approached at about $180\,\mathrm{mm\,s}^{-1}$, compared with 867–$1056\,\mathrm{mm\,s}^{-1}$ for the geometric CBF at these two gains. In forced backup stops during positioning, the clearance loss stayed within 42% of the stopping reserve plus uncertainty allowance for the nominal plant, for pump capacity reduced to 15%, and for combined perturbations at 80% relief pressure. The reserve was exceeded at 50% relief pressure and, under combined perturbations, at 60%, in both cases without adapting the braking ramp; in the reported cases with the ramp scaled to the known capacity, no exceedance occurred. Appendix D details these tests, the parameter perturbations, computation times, and effort accuracy.

7.2. Reaching and docking at 100 collars

A separate MuJoCo campaign on the same plant tested positioning and contact establishment, without drilling, at 100 collars in 50 paired rounds, with 50 targets per boom and 15 assignments across the tunnel center line (Fig. 8). Each operation comprised a move to a 0.45 m stand-off, guarded approach, load establishment, a 2 s docked hold, and retraction. An operation counted as completed only if the total front contact load (stinger plus bit) was at least 4 kN at every controller-cycle sample of the hold. The docking guard still checked the envelope of the intended 4 m hole. The target pattern and route heuristics were refined on the nominal model and in pilot trials; one start-clearance rule was amended during the campaign, and all reported runs use the same final target sequence (Appendix F). Figure 9 shows one recorded round.

The full framework (A) was run under three conditions, S1–S3, which differ in the seeds of the sensing noise, of the directional-valve gains (scattered within ±5% and fixed per run), and of the face relief. Five ablations were run on S1: B removes the online collision rows; C substitutes a kinematic CBF; D uses direct joint-space moves with the full filter; E sets the estimated-error allowances to zero; and F combines direct moves with removed collision rows.

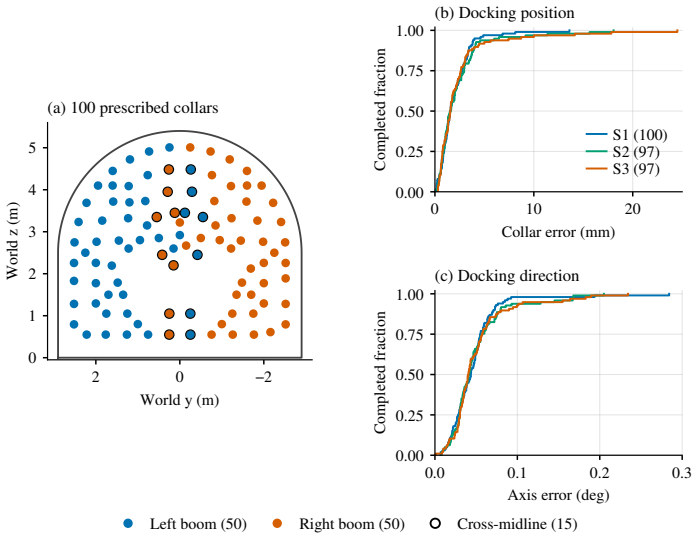

Fig. 8. Target pattern and docking accuracy. (a) Collar locations by assigned boom; rings mark cross-center assignments. (b,c) Empirical cumulative distributions of collar and axis errors at completed docked holds: 100 for S1 and 97 each for S2 and S3. The target sequence is shared across conditions.

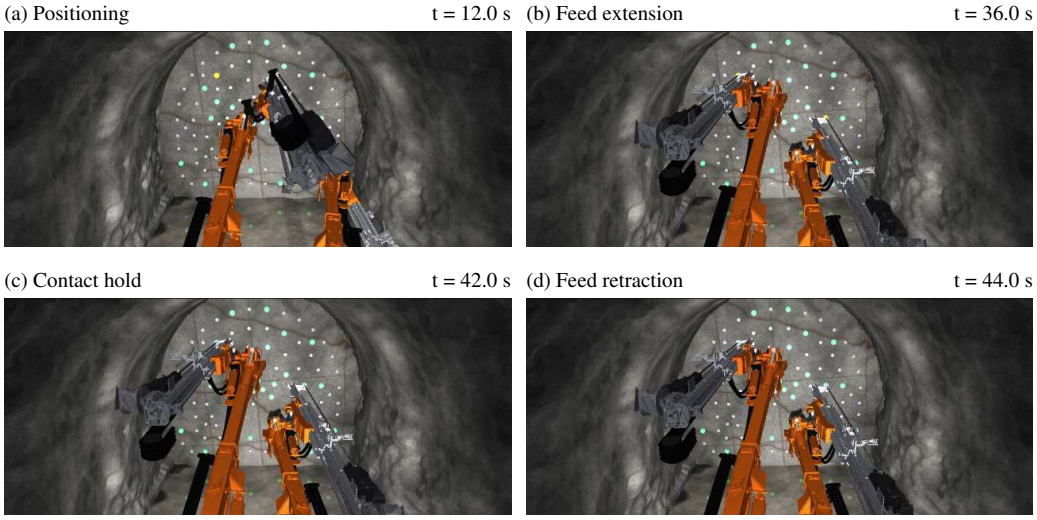

Fig. 9. Recorded MuJoCo execution of round 12 (A/S1, targets L28/R36): positioning, feed extension, supported hold and retraction. Times are relative to the start of the round. All snapshots use the same camera view.

A, B, C, and E share a supervisory look-ahead that uses the full actuator-aware filter, and limit and permitted-contact handling stays active in every variant (Appendix F).

The full framework completed 100, 97, and 97 operations under S1–S3 (294 of 300; 98%) without prohibited contact or sampled policy-clearance violation; the smallest margin over policy was 29.4 mm. Of the six incomplete operations, four belonged to two rounds that were skipped after planning or replanning failed, and two reached the docked hold but fell below the load criterion. Pooled collar errors had a median of 1.57 mm, a 95th percentile of 5.75 mm, and a maximum of 24.51 mm; axis errors had a median of 0.042° and a maximum of 0.284°. For the 94 targets completed in all three conditions, the across-condition range of the collar error had a median of 1.69 mm and a maximum of 23.81 mm. All 296 pre-contact feed-extension rates stayed below 20 mm s^{-1} (maximum 16.5 mm s^{-1}).

Table 3 Outcomes of the 100-collar campaign. N_c counts completed load-qualified docking cycles; N_p counts those completed within paired rounds that retained every monitored policy clearance. $\Delta_{\min}$ is the minimum clearance minus its class policy. $v_{\mathrm{td,max}}$ is maximum feed-extension rate in the 50 ms preceding detected contact; $N_{>20}/N_{\mathrm{td}}$ counts rates above 20 mm s^{-1} among all touch-downs. T is simulated execution time excluding planning computation. D/S1 completed four targets before subsequent direct moves were held by the filter.

Run	N_c	N_p	$\Delta_{\min}$ (mm)	$v_{\mathrm{td,max}}$ (mm/s)	$N_{>20}/N_{\mathrm{td}}$	T (s)
A/S1	100/100	100	+30.8	15.0	0/100	3074.13
A/S2	97/100	97	+30.0	16.5	0/98	3130.51
A/S3	97/100	97	+29.4	15.7	0/98	3060.32
B/S1	100/100	100	+29.4	18.6	0/100	2242.89
C/S1	100/100	100	+26.3	25.9	16/100	2088.09
D/S1	4/100	4	+31.1	10.3	0/4	425.40
E/S1	100/100	100	+30.8	20.3	1/100	2624.52
F/S1	97/100	36	-328.0	14.2	0/98	1570.01

The S1 ablations separate the roles of routing and online filtering (Fig. 10, Table 3). With direct joint-space moves, the full filter (D) preserved every monitored clearance but stalled after four targets, whereas variant F, without the collision rows, completed 97 docking cycles, only 36 of them in policy-compliant rounds, with collision or geometric penetration in 29 rounds and 73.365 s of recorded contact. With supervised routes, A, B, C, and E all

completed 100 targets within the monitored clearances, and B, C, and E needed 15–32% less simulated time than A. Under S1, the look-ahead with the full filter, which these four variants share, thus kept the executed routes within policy even without the online collision rows (B). The online rows preserved clearance when the route was not pre-screened (D versus F), and execution with them took longer (A versus B).

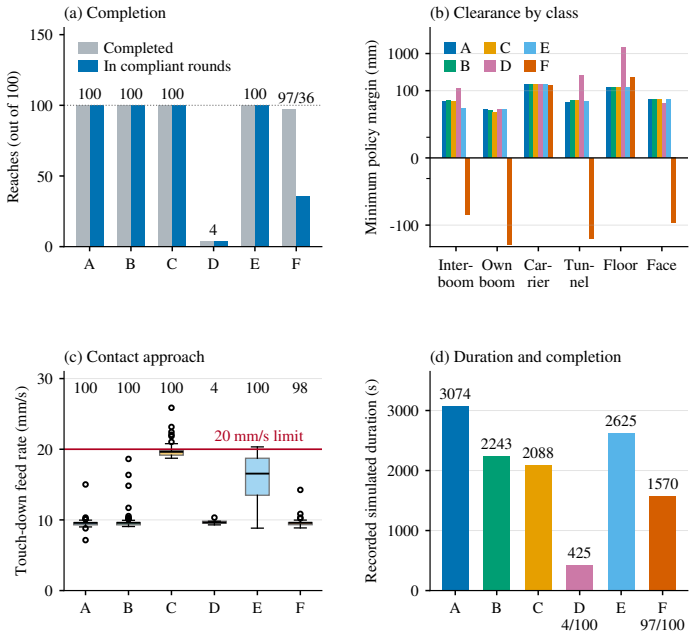

Fig. 10. S1 controller comparisons (A–F: Table F.12): (a) docking completion and completion within policy-compliant rounds; (b) minimum excess over each clearance policy, on a symmetric logarithmic axis; (c) pre-contact feed-extension rates (quartiles, median, 1.5-IQR whiskers and outliers; sample counts above); (d) simulated execution duration, with incomplete task counts marked. Planning computation is excluded.

The online formulations differed in contact approach. The pre-contact feed-extension rate exceeded $20\,\mathrm{mm\,s^{-1}}$ at 16 of 100 touch-downs with the kinematic CBF (C, maximum $25.9\,\mathrm{mm\,s^{-1}}$) and at one of 100 without error allowances (E, $20.3\,\mathrm{mm\,s^{-1}}$), and at none with A or B. Durations in Table 3 are simulated execution time: the plant was paused during route planning, which required a median of 139–167 s of computation per round (Appendix F).

7.3. Cross-engine verification of the exported dual-boom model in Isaac Sim

Cross-engine model verification in Isaac Sim comprised prescribed-state replay, rigid-body tree queries, and a dynamically integrated closed-chain static hold. These checks assessed the transfer of configuration maps, collision geometry, inertia, and equilibrium loads. The replay uses all 17 134 configurations stored at approximately 0.1 s intervals from the demonstration mission. All fifteen checks passed (Table 4).

Table 4 Cross-engine model verification: prescribed-state replay, open-tree dynamics and a closed-chain static hold. Maxima and numerical acceptance criteria refer to the stated samples and channels.

Quantity and coverage	Full-run result	Comparison criterion
Link frames; 17 134 configurations	8.24 μm; 1.34 μrad	1 mm; 1 mrad
Left/right bit position; same configurations	9.10/9.88 μm	1 mm
Loop gap; prescribed-state replay	1.97 μm	1 mm; loops not enforced
Closest-distance discrepancy; 13 classes	1.498 mm	5 mm in $\geq$ 99% of comparable states per class, and for each class minimum
Known-collision controls	6/6 detected	Negative reported separation in every specified collision class
Tree mass matrix; 24 states	$\epsilon_M = 1.75 \times 10^{-5}$	$\epsilon_M < 5 \times 10^{-3}$
Gravity; same 24 states	$\epsilon_g = 8.88 \times 10^{-6}$	$\epsilon_g < 5 \times 10^{-3}$
Coriolis/centrifugal term; same 24 states	$\epsilon_c = 1.20 \times 10^{-5}$	$\epsilon_c < 2 \times 10^{-2}$
Static hold; final second of 10 s	Maximum interval-averaged coordinate speed 2.73×10^{-4} rad/s, 2.42×10^{-5} m/s; loop gap 4.89 μm	Speed over intervals $\geq$ 0.1 s below 10^{-3} rad/s or m/s; gap below 1 mm
Mean body/carrier-coordinate displacement; 12 coordinates	12/12 within tolerance	Larger of 2% of reference magnitude and 20 μrad or 20 μm
Mean actuator effort; 16 force and 4 torque channels	Largest errors 21.4 N and 0.772 N m	Larger of 2% of reference magnitude and 500 N or 500 N m

Figure 11 compares the reference bit paths with positions reconstructed from PhysX link poses. Position and loop-gap discrepancies stayed at the micrometer scale, which confirms the transferred joint frames at the prescribed configurations. Geometric queries covered thirteen distance classes: eleven prohibited contacts and two permitted stinger–face contacts. Every prohibited-contact class kept its policy clearance on the replay grid; the minimum inter-boom separation was 215.13 mm, close to the finer-grid MuJoCo minimum

of 214.76 mm. Six configurations with known self-, inter-boom, roof, floor, carrier, or face collisions produced the expected reports.

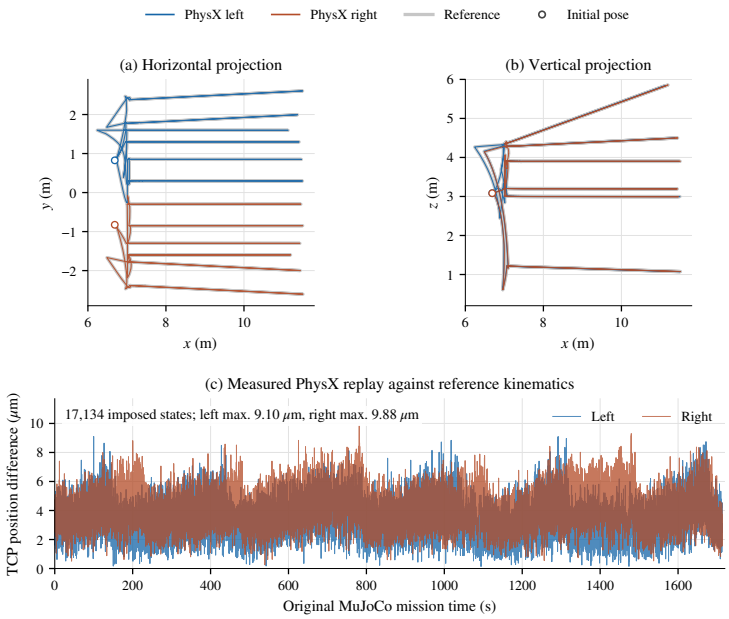

Fig. 11. Prescribed-state verification of bit-tip trajectories. (a,b) Reference kinematics and PhysX link poses at retained MuJoCo configurations. (c) Position discrepancies. Time follows the demonstration mission; gravity and loop enforcement are disabled during replay.

Tree dynamics agreed at twenty-four states after accounting for the armature convention of the two engines. In a separate 10 s closed-chain hold at home with implicit position drives, the final-second mean displacements of all twelve body/carrier response coordinates and the measured efforts of all twenty channels met their tolerances (Appendix E).

8. Conclusion

This paper connected independently compiled closed-chain mechanism models to a centralized CBF-QP that coordinates two hydraulic drilling booms. The program regulates actuator commands and reference progress under mutual, self-, and environmental clearance constraints, nominal effort limits, and per-boom flow budgets; its clearance reserves cover command delay, hydraulic response, braking, residual plant motion, and uncertainty, and a supervisor sequences routing, intentional contact, drilling, and recovery.

In MuJoCo, a twelve-hole mission completed 48.035 m of modeled drilling with mean/maximum collar errors of 1.77/3.98 mm; in separate comparison missions, concurrent operation took 42.5% less simulated time than sequential operation. The 100-collar docking campaign completed 294 of 300 operations across three conditions without sampled policy-clearance violation, with pre-contact feed-extension rates below $20\,\mathrm{mm\,s^{-1}}$ and a pooled median collar error of 1.57 mm. The comparisons indicate a division of roles: supervised routing provided task progress, and the stopping-aware filter preserved clearance when routes were not pre-screened or references conflicted. The comparisons quantify execution duration and contact-approach regulation for the proposed filter and the geometric CBF baseline. Isaac Sim checks confirmed the exported geometry, tree dynamics, and closed-chain static equilibrium.

The capacity-perturbation tests characterize the dependence of stopping reserves on available actuator capacity and braking ramps. The timing results quantify controller and route-planning workloads under the reported computational conditions.

CRediT authorship contribution statement

Mehdi Heydari Shahna: Writing - original draft, Validation, Methodology, Investigation, Formal analysis, Software, Data curation, Conceptualization.

Tuomo Kivelä: Writing - review & editing, Resources, Supervision, Funding acquisition.

Jouni Mattila: Writing - review & editing, Resources, Supervision, Funding acquisition.

Declaration of competing interest

The authors declare that they have no known competing financial interests or personal relationships that could have appeared to influence the work reported in this paper.

Funding

This work was supported by the Finnish Foundation for Technology Promotion (Tekniikan Edistämissäätiö) through the Post Docs in Companies (PoDoCo) program.

Code and model availability

The source code implementing the proposed coordination algorithm can be provided by the corresponding author on reasonable request. Machine-specific model parameters are confidential and are excluded from the shared implementation. Executing the implementation requires separately supplied mechanism, collision-geometry, and actuator-response data.

Appendix A. Hydraulic constitutive model

Chamber continuity and actuator effort satisfy

$$\begin{aligned} &\dot{p}_A = \frac{\beta_e}{V_A(x)}(Q_A - D_A v - Q_\ell), \quad \dot{p}_B = \frac{\beta_e}{V_B(x)}(Q_B + D_B v + Q_\ell), \\ &f^{\mathrm{h}} = D_A p_A - D_B p_B, \qquad f = f^{\mathrm{h}} - f_{\mathrm{fr}}(v), \quad f_{\mathrm{fr}}(v) = F_C \tanh(v/v_s) + b_v v, \end{aligned} \tag{A.1}$$

where $v = \dot{x}$, Q_A, Q_B are signed flows into the chambers, D_A, D_B effective piston/annulus areas, and p_A, p_B chamber pressures. Leakage is $Q_\ell = C_\ell(p_A - p_B)$ with conductance C_ℓ. The effective bulk modulus is β_e; F_C, b_v are Coulomb and viscous friction coefficients, and $v_s > 0$ regularizes the online friction approximation. The plant uses joint friction loss for dry friction. Chamber volumes are $V_A = V_{A0} + D_A(x - x^-)$ and $V_B = V_{B0} + D_B(x^+ - x)$, with dead volumes V_{A0}, V_{B0} and coordinate bounds x^-, x^+. Rotary actuators use displacements per radian for D_A, D_B and torques for f^{h}, f; rod spin has a separate process-drive branch.

The normalized spool opening $\upsilon \in [-1, 1]$ follows $\tau_s \dot{\upsilon} = \upsilon_{\mathrm{cmd}} - \upsilon$, with time constant τ_s and target υ_{cmd}. Compensated metering is

$$\begin{aligned} &Q_{\mathrm{in}} = Q_{\mathrm{nom}}|\upsilon|\phi(p_S - p_{\mathrm{in}}), \quad Q_{\mathrm{out}} = Q_{\mathrm{nom}}\frac{D_{\mathrm{out}}}{D_{\mathrm{in}}}|\upsilon|\phi(p_{\mathrm{out}} - p_T), \\ &\phi(\Delta p) = \frac{d}{\sqrt{p_c(d + p_\epsilon)}}\sqrt{\frac{p_c + p_\epsilon}{p_c}}, \quad d = \mathrm{clip}(\Delta p, 0, p_c), \end{aligned} \tag{A.2}$$

where Q_{nom} is full-opening flow, p_S, p_T supply/tank pressures, p_c the compensator drop, and $p_\epsilon > 0$ the metering regularization. Spool direction selects inlet/outlet pressures $p_{\mathrm{in}}, p_{\mathrm{out}}$, areas $D_{\mathrm{in}}, D_{\mathrm{out}}$, and chamber-flow signs in Eq. (A.1). Load-sensing supply is pump-limited; port relief and make-up functions restrict chamber pressures.

Appendix B. Rock geometry and drilling-load model

The face and local unconfined compressive strength are

$$\begin{aligned} X_f(Y,Z) &= x_f + A_f \operatorname{clip}(\mathcal{F}_2(Y,Z), -1, 1), \\ \sigma(p) &= \sigma_0 \chi_\sigma(p)[1 + a_\sigma \operatorname{clip}(\mathcal{F}_3(p), -1.5, 1.5)], \\ \mathcal{F}_d(p) &= \tfrac{1}{2} \sum_k a_k \cos(\boldsymbol{k}_k^\mathsf{T} p + \psi_k). \end{aligned} \tag{B.1}$$

Here $x_f, A_f, \sigma_0, a_\sigma$ are nominal face location, relief amplitude, intact strength and relative strength variation. Fourier amplitudes a_k, wavevectors $\boldsymbol{k}_k$ and phases ψ_k are seeded. Joint/shear bands use strength factor $\chi_\sigma \leq 1$ and torque multiplier $\chi_T \geq 1$; overlaps take the minimum strength and maximum torque factors. The tunnel has vertical walls, floor $Z = 0$, and a semicircular roof of radius $W/2$ and spring height $H - W/2$, for width W and height H. Piecewise longitudinal expansion represents previous excavation. A discretized face supports frictional stinger contact.

Hammer pressure follows $\tau_h \dot{p}_h = p_h^{\mathrm{cmd}} - p_h$, with time constant τ_h and bounded target p_h^{cmd}. Active percussion gives

$$\begin{aligned} E &= E_0 p_h / p_0, & f_h &= f_0 \sqrt{p_h/p_0}, \\ F_* &= F_{*,0} p_h / p_0, & \eta_F &= \xi e^{1-\xi}, \\ \xi &= F_{\mathrm{ax}} / F_*, & \theta_I &= 180|\omega|/(\pi f_h), \\ \eta_I &= \exp[-(\theta_I - \theta_*)^2/(2s_I^2)], \\ v_p &= \frac{f_h E \eta_F \eta_I}{k_{\mathrm{SE}} \sigma(p_{\mathrm{bot}}) A_{\mathrm{bit}}}. \end{aligned} \tag{B.2}$$

Reference pressure, impact energy, blow frequency and optimal thrust are $p_0, E_0, f_0, F_{*,0}$. Bit thrust and spin are F_{ax}, ω; θ_I, θ_*, s_I are actual/optimal indexing angles and spread in degrees. Bit area is $A_{\mathrm{bit}} = \pi R_{\mathrm{bit}}^2$ for radius R_{bit}; k_{SE} converts strength to specific energy, and p_{bot} is the modeled bottom. Penetration is zero at thrust $F_{\mathrm{ax}} \leq F_{\min}$ or with inactive percussion. Operating hammer flow is $Q_{\mathrm{perc}} = E f_h / (\eta_h p_h)$ for hydraulic efficiency η_h.

For collared unit axis a_0, collar p_{col}, accumulated depth ℓ_h and bit position p_{tip}, compression and axial velocity are $\delta = a_0^\mathsf{T}(p_{\mathrm{tip}} - p_{\mathrm{col}}) - \ell_h$ and $v_a = a_0^\mathsf{T} \dot{p}_{\mathrm{tip}}$. Unilateral contact gives

$$\begin{aligned} F_{\mathrm{ax}} &= \mathcal{C}(\delta, v_a - v_p), \\ \mathcal{C}(\delta, w) &= \begin{cases} [k_a \delta + c_a w \min(1, \delta/\delta_0)]_+, & \delta > 0, \\ 0, & \delta \leq 0, \end{cases} \end{aligned} \tag{B.3}$$

where $[z]_+ = \max(z, 0)$, k_a, c_a are axial stiffness/damping, and δ_0 is the damping-activation range. Scalar bisection couples Eqs. (B.2) and (B.3), advancing the bottom according to contact-dependent penetration. With $r = (I - a_0 a_0^\mathsf{T})(p_{\text{tip}} - p_{\text{col}})$, $\rho = \|r\|$ and $e_r = r/\rho$, wall guidance and initial face friction are

$$\boldsymbol{F}_w = -[k_w(\rho - r_c) + c_w e_r^\mathsf{T} \dot{p}_{\text{tip}}]e_r, \quad \rho > r_c, \quad \boldsymbol{F}_t = \Pi_{\mu_f F_{\text{ax}}}(-k_t s_t - c_t v_t). \tag{B.4}$$

Wall force is zero within clearance r_c; k_w, c_w are wall stiffness/damping. Before wall engagement, s_t, v_t are transverse stick-anchor displacement and velocity, with stiffness/damping k_t, c_t. For friction coefficient μ_f, Π_R projects onto a force ball of radius R. Anchor updates enforce $\|k_t s_t\| \le \mu_f F_{\text{ax}}$ before damping and projection.

Rotational resistance and the rod wrench are

$$\begin{aligned} T_{\text{res}} &= [T_0 \min(1, \ell_h/\ell_0 + b_0) + c_\omega|\omega| \\ &\quad + \mathbf{1}_{F_{\text{ax}} > F_{\min}} \mu_b F_{\text{ax}} r_e \chi_T + T_s] \tanh(\omega/\omega_s), \\ \boldsymbol{F}_{\text{rock}} &= -F_{\text{ax}} a_0 + \boldsymbol{F}_\perp, \\ \boldsymbol{m}_{\text{rock}} &= (p_{\text{tip}} - p_G) \times \boldsymbol{F}_{\text{rock}} - T_{\text{res}} a_{\text{spin}}. \end{aligned} \tag{B.5}$$

Here T_0, ℓ_0, b_0 set initial resistance; $c_\omega, \mu_b, r_e, \omega_s$ define viscous/frictional resistance and stall regularization. The indicator selects loaded friction; T_s adds seeded half-sine jamming pulses in loaded weak rock. The active transverse force is $\boldsymbol{F}_\perp \in \{\boldsymbol{F}_t, \boldsymbol{F}_w\}$, p_G is rod center of mass, and a_{spin} its signed joint axis, including reflection. A separate bore-path model adds joint-induced drift, random wobble and gravity bias while the mechanical rod follows its collared axis.

Appendix C. Tracking maps and sampled barrier diagnostics

Appendix C.1. Transit and terminal tracking maps

For actuator-space reference $x_b^{\text{ref}}(\vartheta_b)$ and clock rate $\dot{\vartheta}_b = s_b$, transit tracking uses

$$\begin{aligned} J_b &= P_{\text{pos}}, \quad w_{\text{ff},b} = P_{\text{pos}}\, dx_b^{\text{ref}}/d\vartheta_b, \\ w_{\text{fb},b} &= \text{clip}\Big(K_x P_{\text{pos}}(x_b^{\text{ref}} - x_b), -\bar{w}_b, \bar{w}_b\Big). \end{aligned} \tag{C.1}$$

The selector $P_{\text{pos}} = [I_6\ 0_{6\times 3}]$ retains six positioning coordinates, K_x contains proportional gains, and $\bar{w}_b$ bounds feedback componentwise. With $\Pi_{\text{pos}} =$

$P_{\text{pos}}^{\mathsf{T}} P_{\text{pos}}$, terminal alignment uses

$$J_b = \begin{bmatrix} J_{p,b} \\ \beta_{b1}^{\mathsf{T}} J_{\omega,b} \\ \beta_{b2}^{\mathsf{T}} J_{\omega,b} \end{bmatrix} \Pi_{\text{pos}}, \quad w_{\text{fb},b} = \begin{bmatrix} K_p(p_b^d - p_b) \\ K_o \beta_{b1}^{\mathsf{T}}(a_b \times a_b^d) \\ K_o \beta_{b2}^{\mathsf{T}}(a_b \times a_b^d) \end{bmatrix}. \tag{C.2}$$

Here p_b, a_b denote estimated tool position and unit axis; p_b^d, a_b^d are their targets. Orthonormal β_{b1}, β_{b2} span the plane perpendicular to a_b^d, with gains $K_p, K_o > 0$. Translation/orientation feedback is bounded and attenuated near poor task-map conditioning. Terminal feedforward is zero; tool roll enters the secondary preference. Positioning-actuator columns alone determine terminal alignment.

Appendix C.2. Sampled barrier recursion and effort discrepancy

For a row with the same definition in consecutive cycles, the inter-cycle prediction defect is

$$\delta_{i,k} = \widehat{H}_i^{(2)}(c_k)\Big|_k - \widehat{H}_i^{(1)}\Big|_{k+1}. \tag{C.3}$$

When the optimized command is applied and Eq. (19) is inactive, Eq. (18) implies

$$\widehat{H}_i^{(1)}(k+1) \geq \min\left\{(1-\gamma\Delta t_k)\widehat{H}_i^{(1)}(k),\, \widehat{H}_i^{(2)}(c_k^{\text{br}})\Big|_k\right\} - \delta_{i,k}. \tag{C.4}$$

The measured defect combines response and integration errors, changes in witnesses and estimates, and local-reserve variation. The values reported in Appendix D characterize the sampled barrier recursion. Extension to a plant-level invariance result additionally requires a uniform bound on $\delta_{i,k}$. A mode change restarts the recursion with the new barrier, including stopping terms for released actuators, and a change of control period requires valid prediction and stopping bounds for the new period; the barrier jumps observed at such transitions are also reported there.

For Eq. (22), robust effort limits take the form $F_{b,j}^{+} - \varepsilon_{b,j}$ and $F_{b,j}^{-} + \varepsilon_{b,j}$ when $\varepsilon_{b,j}$ bounds the complete-period discrepancy between predicted and actual effort, including pressure transients and external loading. The effort errors measured in the tested conditions are given in Appendix D; capacity-aware stopping additionally uses the available pressure, flow, and realizable ramp.

Appendix D. Detailed drilling outcomes and controller diagnostics

Appendix D.1. Task, plant and individual outcomes

The tunnel width and height were 5.8 and 5.4 m. The face was centered at $X = 7.45$ m with 0.12 m relief amplitude; world axes point toward the face (X), left (Y), and upward (Z). Target collars were ray–surface intersections. Table D.5 spans central cut holes separated by 0.6 m, asymmetric 20° upward drilling, and outward contour/corner configurations.

Table D.5 Six-round target pattern. (Y_0, Z_0) are ray-anchor coordinates in meters at $X_0 = 7.45$ m; collars are intersections with the nonplanar face. Yaw is positive from $+X$ toward $+Y$, elevation upward. Each target depth is 4.0 m.

Round	Left hole: type; (Y_0, Z_0)	Right hole: type; (Y_0, Z_0)	Yaw L/R (°)	Elevation L/R (°)
1	Production; $(1.30, 3.20)$	Production; $(-1.30, 3.20)$	0/0	0/0
2	Upward; $(1.60, 4.50)$	Production; $(-0.85, 3.90)$	0/0	20/0
3	Central cut; $(0.30, 3.00)$	Central cut; $(-0.30, 3.00)$	0/0	0/0
4	Production; $(0.85, 3.90)$	Upward; $(-1.60, 4.50)$	0/0	0/20
5	Roof contour; $(1.80, 4.30)$	Roof contour; $(-1.80, 4.30)$	$+2.86/-2.86$	$+2.86/+2.86$
6	Lower corner; $(2.40, 1.20)$	Lower corner; $(-2.40, 1.20)$	$+2.86/-2.86$	$-1.72/-1.72$

The hydraulic model in Section 3 was coupled to the rock/contact model in Appendix B. Rock parameters were prescribed at 200 MPa intact strength and 6% field scaling, with three joint families, one shear band and a 64 mm bit. Control used actuator/carrier measurements and estimated orientation corrections; evaluation used plant states. Rock, sensing, and left/right torque-event seeds were 2026, 11 and 77/78; bore-path seeds for zero-based round r were $1000 + 10r$ and $1001 + 10r$.

The missions were run with MuJoCo 3.3.7 (implicit-fast integrator, Newton solver with at most 100 iterations and tolerance 10^{-10}, elliptic friction cones) under Python 3.11 with NumPy 2.4.4; distance queries used Coal 3.0.3. The QP was solved in dense form by the dual active-set method of Goldfarb and Idnani [26] (quadprog 0.1.12), cold-started in every cycle. Decision variables were scaled by nominal actuator speed, flow, and ramp travel, constraint rows by their largest coefficient, and the Hessian was regularized by 10^{-6} times its mean diagonal. A solution was accepted when the largest scaled constraint violation was below 10^{-6}; otherwise the cycle counted as a solver failure. Rows satisfied by every admissible command were removed before the solve. Table D.6 lists the controller and response parameters.

Collar and axis errors at hole definition were

$$e_{p,h} = \|p_h - p_h^\star\|_2, \qquad e_{a,h} = \cos^{-1}\left(a_h^\top a_h^\star\right), \tag{D.1}$$

Table D.6 Controller and response parameters of the reported missions. Actuator order: swing, lift, zoom, tilt, feed-swing, roll, bolting, feed extension, feed. The bolting cylinder is not actuated in the missions and uses the tilt-cylinder values.

Quantity	Value
Response times τ_{bj} (ms)	78, 66, 44, 69, 62, 116, 69, 44, 45
Identified lag T_j/ι (ms)	126, 107, 66, 125, 138, 128, 125, 68, 61
Response inflation ι	1.25 (twelve-hole missions); 1.30 (100-collar campaign)
Slew bounds a_{bj}	$0.15\,\mathrm{m\,s^{-2}}$; roll $1.0\,\mathrm{rad\,s^{-2}}$; feed extension and feed $0.6\,\mathrm{m\,s^{-2}}$
Rate limit; ramp majorant	0.6 of nominal valve speed; four linear segments
Capacity reserves η_v, η_Q	0.8, 0.9
residual-response decay time $\tau_{\mathrm{ring},j}$	3 s
γ; η_b; h_{fb}; κ_d	$20\,\mathrm{s^{-1}}$; 0.5; 10 mm; $200\,\mathrm{m^{-1}}$
Model updates	reduced dynamics and geometry correction every five control cycles
$\epsilon_{x,j}$	0.2 mm (strokes); 0.5 mrad (roll)
Per-axis error bounds	orientation correction 2.5 mrad; carrier 0.5 mm and 0.1 mrad
ρ_i	face interpolation 4 mm; linearization 1 mm; row-specific geometry terms
Contact	$\bar{v}_c = 20\,\mathrm{mm\,s^{-1}}$; $d_c = 5\,\mathrm{mm}$; $F_{\mathrm{st,min}} = 4\,\mathrm{kN}$; $F_{\mathrm{bit,max}} = 20\,\mathrm{kN}$
Tracking	$K_p = K_o = 2.5\,\mathrm{s^{-1}}$ (bounds $0.1\,\mathrm{m\,s^{-1}}$, $0.1\,\mathrm{rad\,s^{-1}}$); $K_x = 3\,\mathrm{s^{-1}}$; $\rho_b = 100$
Supervisor	look-ahead step 20 ms; stall after 3 s below 1% of nominal rate and 5% clock rate; at most two replans

where p_h and a_h are actual collar position and unit axis, and starred quantities are targets. Table D.7 separately reports the rock model's transverse bottom drift from the collared axis.

Table D.7 Individual outcomes of the demonstration mission. Collar and axis errors follow Eq. (D.1); bottom drift is the rock-model offset from the collared straight axis. Duration spans hole definition after support loading through flushing, including rapid feed, collaring, drilling and recovery. All holes reached their targets.

Hole	Depth (m)	e_p (mm)	e_a (°)	Bottom drift (mm)	Duration (s)	Anti-jamming activations
1L	4.0028	1.51	0.014	73.1	123.7	0
1R	4.0027	3.98	0.034	65.4	210.8	19
2L	4.0025	3.89	0.034	16.9	172.1	7
2R	4.0026	0.62	0.015	79.6	211.0	17
3L	4.0028	1.71	0.028	123.9	249.7	26
3R	4.0027	1.74	0.049	77.3	254.9	26
4L	4.0056	1.17	0.015	53.6	169.8	8
4R	4.0027	0.90	0.069	31.3	246.4	22
5L	4.0028	2.15	0.024	29.2	126.2	0
5R	4.0029	0.90	0.005	70.0	302.1	36
6L	4.0027	1.46	0.025	37.5	135.8	1
6R	4.0025	1.14	0.004	56.2	144.1	3

Appendix D.2. Clearance, hydraulic demand and contact

Table D.8 and Fig. D.12 detail the demonstration mission. Minimum inflated barrier and stopping guard were -5.75 and $+4.72$ mm, with a 10 mm recovery band. The largest clearance-estimation error divided by its allowance, excluding this band, was 0.408. The per-axis orientation-correction error bound was 2.5 mrad, which gives $\epsilon_\theta = \sqrt{3} \times 2.5 = 4.33$ mrad in Eq. (13). The largest residual component was 2.18 mrad and the largest residual norm 2.26 mrad. Peak flow utilization was 0.486, with no force-limit relaxation; at most 389 barrier rows were constructed and 132 retained per QP.

Table D.8 Minimum monitored clearances, taking the smaller value across booms. Policies apply to active collision pairs; designated tool–rock contacts and structural exclusions follow their respective contact rules.

Class	Policy (mm)	Minimum (mm)	Margin (mm)
Inter-boom	50	214.8	164.8
Active self-pairs	30	79.1	49.1
Carrier	50	198.5	148.5
Tunnel walls/roof	100	259.8	159.8
Floor	100	513.4	413.4
Nonpermitted face	30	86.5	56.5

Pre-contact speeds were evaluated over 0.3 s before front-contact/collaring transitions. At contact detection, the largest absolute estimated gap divided by its error allowance was 0.14. Left/right bit-force peaks reached 20.95/23.01 kN, while maximum transverse stinger-tip displacement was 3.45 mm.

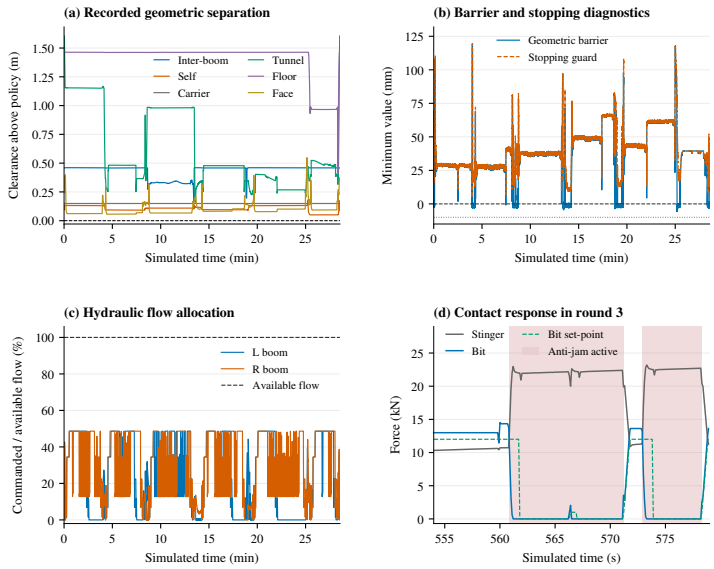

Fig. D.12. Demonstration mission: (a) clearance above each active class policy; (b) minimum inflated barrier and stopping guard, with the $-10\,\mathrm{mm}$ recovery boundary; (c) flow normalized by available supply; and (d) left-boom contact forces, bit-force target and shaded anti-jamming intervals in round 3. Contact traces are sampled at $10\,\mathrm{Hz}$; peak forces in the text use full-rate measurements.

Appendix D.3. Conflicting references and parameter perturbations

The geometric CBF used velocity-level geometric constraints in place of the proposed stopping reserve, actuator-response prediction, slew and braking treatment and hydraulic rows. An additional twelve-hole mission at $0.3\,\mathrm{m}$ depth also completed without inter-boom contact when inter-boom filtering and planning checks were removed.

Conflicting references drove both booms across the tunnel center with supervision bypassed. Closing speed used a centered $0.1\,\mathrm{s}$ distance secant at the first $200\,\mathrm{mm}$ separation (Fig. D.13). Proposed half/full-speed tests approached at approximately $180\,\mathrm{mm\,s^{-1}}$. The geometric CBF at $\gamma = 20\,\mathrm{s^{-1}}$ approached at $889/1056\,\mathrm{mm\,s^{-1}}$, reaching $0.88/-0.62\,\mathrm{mm}$ minimum separation; the full-speed case recorded contact over twelve $1\,\mathrm{ms}$ steps. Removing inter-boom information also produced contact. At $\gamma = 5\,\mathrm{s^{-1}}$, the geometric CBF kept $75.22/77.15\,\mathrm{mm}$ at $867/983\,\mathrm{mm\,s^{-1}}$. Slowing the reference with $\gamma = 20\,\mathrm{s^{-1}}$ kept $55.29\,\mathrm{mm}$ at $321\,\mathrm{mm\,s^{-1}}$. These cases show gain sensitivity and conservative speed regulation, including the effect of constraints from the nearby face.

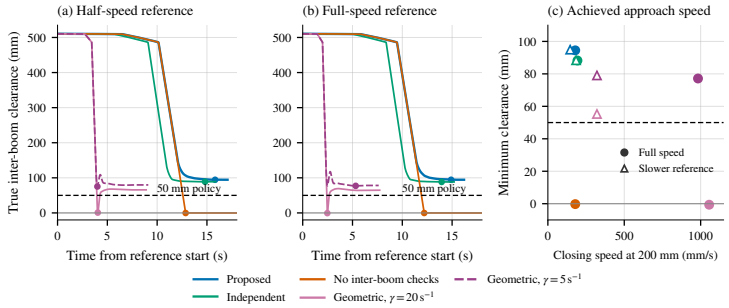

Fig. D.13. Conflicting references with route supervision bypassed: (a,b) inter-boom clearance during the first 18 s at half/full reference speed, with the 50 mm policy dashed; (c) achieved approach speeds for full and slower schedules, the latter lasting 5.5 times longer. Closing speed uses a centered 0.1 s interval at the first 200 mm crossing.

Increasing one valve gain by 15% and reducing the other pump capacity to 35% left 94.80 mm clearance with the proposed filter at 204 mm s^{-1}. In separate two-round, 0.3 m missions with both valve gains increased by 15%, its maximum support-approach speed was 9.5 mm s^{-1}. The geometric CBF reached 21.9 mm s^{-1} at support approach and 21.1 mm s^{-1} at collaring, against the 20 mm s^{-1} limit. Both drilled four holes; the geometric CBF returned home, while the return-home route of the proposed controller was rejected.

Appendix D.4. Computation and overrun-conditioned commands

The controller-core time is the wall-clock duration of one complete controller update, from the sampled measurements to the returned commands and progress rates. It comprises closure reconstruction and motion maps, orientation correction estimation, distance queries and constraint rows, the tracking and reduced-dynamics terms, and both assembly and solution of the QP, including the guard evaluation. The demonstration mission had mean/99th-percentile core times of 35.7/56.4 ms. Table D.9 reports separate reference and accelerated evaluations. Full accelerated 0.3 m missions used one numerical-library thread with dedicated computational resources; the accelerated 4 m round used default threading, and reference timing shared resources with another mission. The reported timings characterize controller-core workload under the stated hardware, threading, and resource-sharing conditions.

Overrun-conditioned substitution completed twelve 0.3 m holes in 489.08 s with three replans and no prohibited contact, compared with 452.57 s and one replan without substitution. All 2154 post-startup 50 ms cycles were

Table D.9 Measured 10 ms controller-core cycles. Full accelerated missions use 0.3 m holes; the accelerated 4 m test covers round 3. Substitution follows a detected overrun before the next synchronous plant step. The first two startup cycles are excluded; reference statistics also exclude one recorded cycle exceeding 1 s.

Run	Cycles	Mean (ms)	P99 (ms)	Max. (ms)	Over 10 ms
Reference, full 4 m mission	45 249	34.49	83.50	271.26	45 249 (100%)
Accelerated, full 0.3 m, no substitution	34 497	5.79	9.80	22.79	275 (0.797%)
Accelerated, full 0.3 m, substitution	38 141	5.83	9.98	35.77	375 (0.983%)
Accelerated, round 3 at 4 m	8 482	6.09	10.09	25.70	90 (1.061%)

within period, with a 10.41 ms maximum. The 377 substitutions included two startup cycles of 59.07 and 62.74 ms.

Because the plant is stepped synchronously, the braking command was substituted after computation and reference-clock advancement and before the next plant step; deployment with a continuously evolving plant requires an independently scheduled fallback and coordinated clock updates. Numerical comparison of reference and accelerated evaluations satisfied 86 of 88 checks. Two command differences exceeded the 10^{-5} normalized tolerance, with maximum discrepancy 5.64×10^{-5} of nominal valve speed.

Appendix D.5. Actuator-effort accuracy

Predictions from Eq. (22) were compared with $f_j^{\mathrm{h}} = D_{A,j}p_{A,j} - D_{B,j}p_{B,j}$, sampled every 1 ms and averaged over a command period. The error, in percent of port-relief effort, was $100|\langle f_j^{\mathrm{h}}\rangle - \widehat{f}_j^{\mathrm{h}}|/\max(|F_j^-|, |F_j^+|)$. Alignment included the one-period delay and retained complete, unchanged-mode periods (Table D.10).

Table D.10 Maximum effort discrepancy normalized by port-relief effort. The first six rows compare nominal acceleration-effort predictions with period-mean chamber effort. Loaded closed-boom rows report chamber effort beyond rigid-model gravity; boom and feed groups are separate.

Condition	Error (%)
Nominal mission, free motion: boom actuators	3.10
Nominal mission, free motion: feed actuators	5.76
Dedicated nominal test: imposed ramp braking	4.78
Dedicated nominal test: abrupt valve closure	7.88
Unknown 300 kg payload per drill: ramp braking	18.64
Unknown 300 kg payload per drill: valve closure	20.12
Loaded drilling: closed boom actuators	39.0
Loaded drilling: rate-commanded feed	44.6

Nominal boom inertial correction peaked at 2.90% of relief effort, placing most free-motion demand in the gravity/friction contribution. Braking-row discrepancies relative to the first post-closure chamber-effort mean reached 9.8% nominally and 12.3% with known 300 kg payloads. Loaded-operation discrepancies quantify additional effort beyond the rigid positioning approximation. Nominal missions used the untightened effort rows and standard braking ramp.

Appendix D.6. Backup stops and capacity dependence

During positioning toward round 3, 3 s backups were imposed every 5 s. Inter-boom, self and carrier distances were monitored by active row; tunnel, floor and face distances used class minima. Utilization is the loss from committed-state estimated distance to minimum monitored stop distance, divided by the uninflated stopping reserve plus uncertainty allowance excluding the recovery band. Values above one identify reserve exceedance (Table D.11).

Table D.11 Forced-backup tests. Each row–stop check follows one collision row during one stop. Known/unknown denotes whether reduced relief settings are supplied to the controller. Combined conditions add 300 kg per drill, set pump capacity to 35%, increase valve gain by 15%, and apply sensor bias at its assumed bounds. Relief percentages are relative to nominal settings.

Condition	Stops	Row–stop checks	Exceedances	Max. utilization	Requested move
Nominal plant	19	795	0	0.36	Completed
Pump capacity 15%, unknown	19	703	0	0.42	Completed
Combined; relief 80%, unknown	16	507	0	0.40	Completed
Relief 50%, unknown	51	8950	15	2.84	Failed
Relief 50%, known; widening only	21	1476	17	3.27	Failed
Combined; relief 60%, unknown	9	259	22	6.92	Failed
Relief 50%, known; scaled ramp	13	228	0	0.35	Declined†

†The requested round was rejected; reported stops occurred during the subsequent return home. Additional configurations assessed known payload and combined known capacity.

Nominal stops reached standstill within 0.69 s. Successful tests with adequate pressure headroom began at estimated rates up to 0.44 of nominal valve speed, within the filter's 0.6 limit. Capacity reductions identify the operating boundary: at 50% relief, reserve exceedances occurred with both unknown limits and known limits using force-row widening. Under combined perturbations at 60% relief, roll holding capacity was lost before braking and monitored self-clearance reached approximately −185 mm. This geometric monitor captures within-boom overlap independently of the plant's inter-body contact counter.

With known capacity, an optional slower ramp increased reserved travel. At 60% relief without combined perturbations, the requested move completed with a ramp factor up to 4.11 and no reserve exceedance. More severe known-capacity cases were rejected in planning, with subsequent return/hold outcomes reported separately. These tests used capacity adaptation in addition to the nominal controller.

Appendix D.7. Barrier and recovery diagnostics

The proposed concurrent run in Table 2 completed 69 537 successful QP cycles, with minimum inflated barrier −5.16 mm, minimum stopping guard +3.95 mm, and maximum clearance-error/allowance ratio 0.474. In unchanged-mode 10 ms cycles, next-cycle shortfall from the previous target had 1.43 mm 99th percentile and 4.60 mm maximum. At hold-mode transitions, minimum barrier decreased by up to 28.6 mm, remaining positive immediately afterward. These sampled values show how closely the recursion in Eq. (C.4) held, including the effect of contact-induced motion of nominally closed actuators.

Policy-clearance steps of 6/9 mm created approximately 3/6 mm barrier deficits; first nonnegative returns occurred after 0.15/0.23 s. A 40 mm step activated the guard for two cycles. Inter-boom separation remained above 97 mm.

Appendix E. Cross-engine verification protocol

The exported representation contains 63 rigid bodies, 60 tree coordinates (37 revolute and 23 prismatic), two fixed tree joints and ten loop joints, including ten auxiliary links of total mass 0.10 kg. Collision geometry comprises 256 convex pieces, four capsules, forty boxes and one face mesh, with 305 filtered link pairs. Body and joint names, quaternion conventions and coordinate signs were matched before comparison. Tests used Isaac Sim 5.1.0 with CPU physics.

Prescribed-state geometry. Each retained configuration was assigned with gravity and loop enforcement disabled. Link poses and contacts were sampled after a 1 ms step and one manifold-refresh step. GJK closest-distance queries used PhysX poses and cooked hulls; Coal reference queries used the exported shapes. Conversion of 156 controller convex pieces to 256 exported pieces introduced at most 3.20 mm reduction deviation; cooking added at most 4.23 mm inward deviation. All cooked hulls were available, and the remaining shapes retained their authored geometry.

Closest-distance agreement and contact reporting were evaluated separately. Initial left-face manifold separation lay up to 108.2 mm below the reference distance. After refresh, all thirteen classes were reported at every comparable state, with separation-minus-reference differences from -0.184 to $+57.86$ mm. Figure E.14 compares these quantities.

Tree dynamics. Queries at 24 stored states used disabled loops and collisions. For MuJoCo and PhysX mass matrices M^{MJ} and M^{PX}, and diagonal MuJoCo armature A,

$$\epsilon_M = \max_{k,i,j} \frac{\left| M_{ij}^{\mathrm{PX}}(k) - \left(M^{\mathrm{MJ}}(k) - A \right)_{ij} \right|}{\sqrt{M_{ii}^{\mathrm{MJ}}(k) M_{jj}^{\mathrm{MJ}}(k)}}. \tag{E.1}$$

The target excludes armature, while normalization retains the recorded MuJoCo diagonal; retaining armature in the target gives approximately 0.908. Gravity and Coriolis errors use $\epsilon_f = \max_k \|f^{\mathrm{PX}}(k) - f^{\mathrm{MJ}}(k)\|_\infty / \|f^{\mathrm{MJ}}(k)\|_\infty$ with matched signs and fixed SI coordinates.

Closed-chain equilibrium. The home hold enabled gravity and all ten loops, using the prescribed load-dependent support model, implicit position drives, a 1 ms step, 64 position iterations and one velocity iteration. External forces were applied at every solver iteration. Friction and limits were disabled; drives held actuator and coupled feed coordinates at home, with equality holders in MuJoCo.

Final-second excursions were bounded by 36.1 μrad and 3.58 μm. Table 4 uses position-derived speeds over ≥ 0.1 s; angular maxima over 0.02 s and instantaneously were 1.27×10^{-3} and 8.97×10^{-3} rad/s. Equilibrium efforts average every final-second step. The 16 force and four torque channels include lift/tilt cylinders at approximately 132.3/15.1 kN each. The 2% tolerance governed the lifts; absolute tolerances governed the other eighteen channels, including sixteen lightly loaded channels. Force standard deviation reached 10.2 kN. Measured joint efforts passed all twenty mean-load comparisons; the drive spring component passed eight.

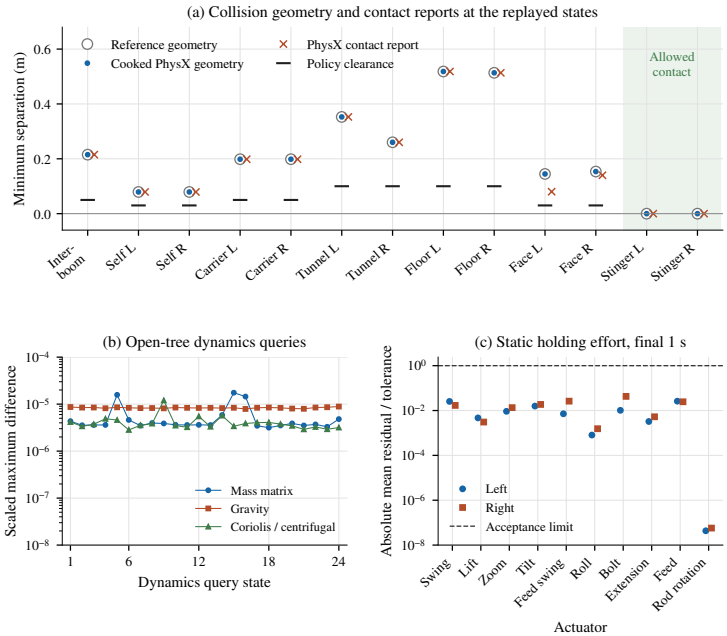

Fig. E.14. Cross-engine diagnostics: (a) closest distances and contact reports for eleven prohibited classes and two permitted stinger contacts; (b) open-tree dynamics with armature excluded from the reference matrix; (c) final-second mean effort residuals divided by channel tolerance (threshold: unity).

Appendix F. Protocol and diagnostics of the 100-collar campaign

Appendix F.1. Target selection, conditions and completion

The 100-collar pattern was adapted to the modeled rig through nominal-model reachability, entry/exit and docking checks: 23 collars were relocated, and 15 were assigned across the center line. Target and access checks covered all three face reliefs; dynamic look-ahead screening used S1. The paired order exercised conflicting transitions and varied postures. The 4 m depth parameter defined the remaining-drilling envelope checked before feed extension; each executed operation comprised positioning, docking, holding and retraction.

Conditions S1, S2 and S3 used seed tuples for sensing, valves and face relief of $(11, 101, 2026)$, $(12, 102, 2027)$ and $(13, 103, 2028)$. Directional-valve gains were independently drawn from $[0.95, 1.05]$ and held fixed per run, while the controller used nominal gains. The pressure-controlled feed-extension branch retained its nominal mapping. The campaign used a 1.30 stopping-reserve multiplier, compared with 1.25 in the twelve-hole mission. The former is a prescribed design reserve motivated by $1.229 \times 1.05 \simeq 1.290$.

Load establishment required front force above 70% of the 10 kN loading target after at least 1 s in the loading phase, with feed extension below $2\,\mathrm{mm\,s^{-1}}$ for 0.05 s. Completion required the full 2 s hold, total stinger-plus-bit load of at least 4 kN at every controller-cycle hold sample, and retraction. This process criterion was evaluated separately from placement accuracy and clearance compliance. S2 round 39 and S3 round 20 each contributed two skipped targets after planning/replanning failed. S2 round 31 and S3 round 25 each contributed one right-boom hold with a recorded zero-load sample. The resulting counts are 100/97/97 for A. F likewise had one below-threshold hold, plus two rejected docking geometries. The criterion is evaluated at every controller cycle and therefore detects brief load drops that fall between stored trajectory samples.

Appendix F.2. Controller variants and supervisory refinement

Table F.12 Controller configurations in the 100-collar campaign. Supervised variants A, B, C and E all evaluate candidate routes with the full actuator-aware filter. All variants retain phase supervision, actuator command bounds, stroke/joint limits and pre-extension docking guards.

Variant	Route selection	Online control
A	Supervised	Full actuator-aware collision, effort and permitted-contact constraints.
B	Supervised	Collision classes removed; limit, effort, valve/flow, slew and permitted-contact constraints retained.
C	Supervised	Kinematic CBF with $\gamma = 20\,\mathrm{s}^{-1}$, valve/flow bounds and kinematic permitted-contact constraints.
D	Direct	Full actuator-aware filter; direct joint-space references.
E	Supervised	Full filter with estimated-error/geometry allowances set to zero, including the contact-gap allowance; recovery band and stopping inflation retained.
F	Direct	Same retained online constraints as B; direct joint-space references.

For C, the geometric/limit rows use $Gc \geq -\gamma \max(d - D, 0)$, with policy distance D for collision rows and zero for limits. G stacks the actuator-coordinate constraint gradients, and the inequality acts componentwise. This formulation regulates geometric velocity and contact approach; the full formulation additionally represents delayed actuator response, slew/braking, nominal effort and uncertainty allowances. E keeps the 10 mm recovery band and the 1.30 stopping inflation, and its phase supervision still uses the full gap-uncertainty calculation. The geometric CBF of the twelve-hole mission kept its stated uncertainty allowances. A, B, D, and F form a two-factor comparison of supervision and online collision rows, with their other constraints in common.

Pilot trials refined the target rolls and supervisory rules before the reported comparisons. The study-specific supervisor in Section 6 added a 4.33 mrad planning reserve to ϵ_θ in its look-ahead, for all rows except the inter-boom rows. Its look-ahead screened persistent slow progress at 3% of nominal actuator speed and 15% reference-clock rate for 3 s, then evaluated alternative routes. Pilot outcomes were excluded from the campaign statistics.

One start-clearance rule was amended during the reported campaign. The final precheck uses its nominal 100 mm inter-boom threshold when the starting separation meets that threshold; otherwise the threshold is $\max(50\,\mathrm{mm}, d_0 - 5\,\mathrm{mm})$, where d_0 is the initial separation. C was restarted, A/S2 continued from its saved state at 1640 s, and A/S3 and E used the amended rule. The completed A/S1 and B runs were kept because none of their recorded planning calls started in the amended condition, and D and F use direct references. All eight reported runs share the final target sequence.

Appendix F.3. Placement and geometric monitoring

Table F.13 Accuracy and contact statistics. Collar and axis entries are median/95th percentile/maximum over completed holds. Peak stinger/bit forces are separated; minimum front load uses recorded samples from completed holds, and slip is maximum transverse stinger motion.

Run	Collar error (mm)	Axis error (°)	Peak forces (kN)	Min. load (kN)	Max. slip (mm)
A/S1	1.56/4.01/13.60	0.044/0.083/0.284	19.2/18.2	8.71	0.23
A/S2	1.58/6.08/18.06	0.041/0.132/0.205	23.3/18.9	8.76	0.26
A/S3	1.56/7.70/24.51	0.041/0.116/0.234	19.8/15.1	8.45	1.78

Table F.13 lists the accuracy and contact statistics of the full framework, and Fig. F.15 compares the three conditions. The 294 completed holds form a pooled descriptive sample, with 94 targets common to all three missions.

Clearances were evaluated at controller cycles using plant body poses. Stored 0.1 s windows retain each class minimum; collision contacts were recorded at the 1 ms plant step. Table F.14 and Fig. F.16 show the resulting sampled geometric envelope. For A, 908 886 filter cycles had no guard or solver fallback; maximum measured clearance-error/allowance ratios were 0.91, 0.49 and 0.85 across S1–S3.

A separate triangle-mesh audit evaluated inter-boom, same-boom and carrier pairs at 9223, 3131 and 3061 configurations in A/S1–S3, respectively, and found no intersecting pair. B, C, D, and E likewise had no intersection over 1122, 1045, 426 and 1313 audited states. Audited minimum inter-boom

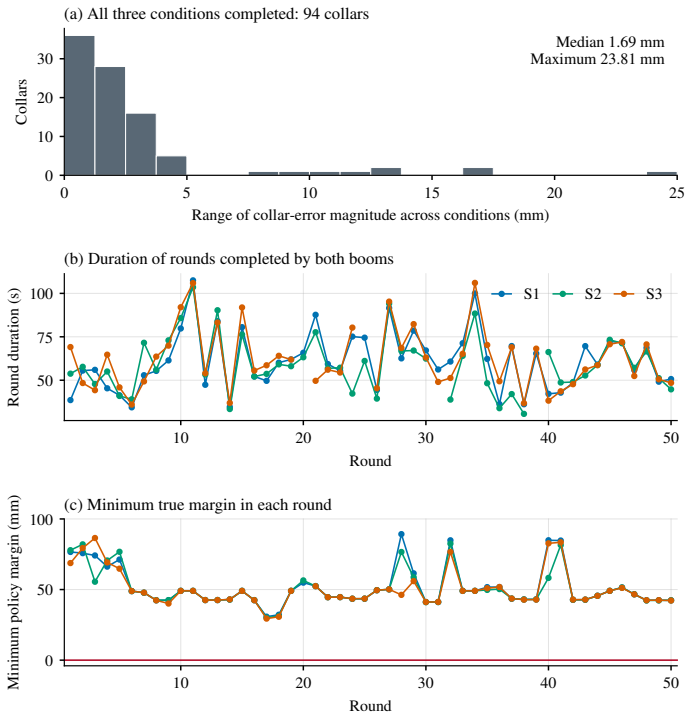

Fig. F.15. Full-framework condition sensitivity: (a) range of collar-error magnitude across S1–S3 for the 94 targets completed in all conditions; (b) durations of rounds completed by both booms; (c) minimum clearance excess over policy in each round. Conditions jointly vary sensing noise, valve gains and face relief.

Table F.14 Minimum monitored clearance in millimeters, with class policy in parentheses. Distances use plant configurations and active convex collision geometry; designated contact pairs follow their permitted-contact rules.

Run	Inter-boom (50)	Self (30)	Carrier (50)	Tunnel (100)	Floor (100)	Face (30)
A/S1	101.2	60.8	195.4	148.7	224.6	89.3
A/S2	94.9	60.0	189.6	173.1	160.8	88.9
A/S3	100.9	59.4	197.5	171.0	306.4	70.1
B/S1	103.3	59.4	194.9	155.8	226.0	89.2
C/S1	101.1	56.3	195.3	155.7	225.3	89.2
D/S1	162.7	61.1	198.5	362.8	1527.6	74.3
E/S1	82.4	60.8	195.3	151.2	225.3	89.2
F/S1	-0.6	-298.0	191.5	-131.4	321.4	-57.6

mesh distances for A were 126, 122 and 122 mm; the controller's enclosing

convex geometry produced the smaller sampled distances in Table F.14. Environmental clearance used the plant-geometry monitor. Within-boom overlap was evaluated geometrically.

F recorded 73.365 s of plant contact, 122.12 s of monitored penetration and 158.05 s below at least one policy distance. Its policy-violation durations by class were 27.54/49.71/72.67/18.45 s for inter-boom/self/tunnel/face; these intervals can overlap. The final return home contributed 1.91 s of penetration outside the paired rounds. A focused triangle audit over 3105 event-window states found 29 intersecting body pairs: one inter-boom and 28 within-boom pairs. This count and the 29 affected rounds are different groupings of the same events and coincide only in number.

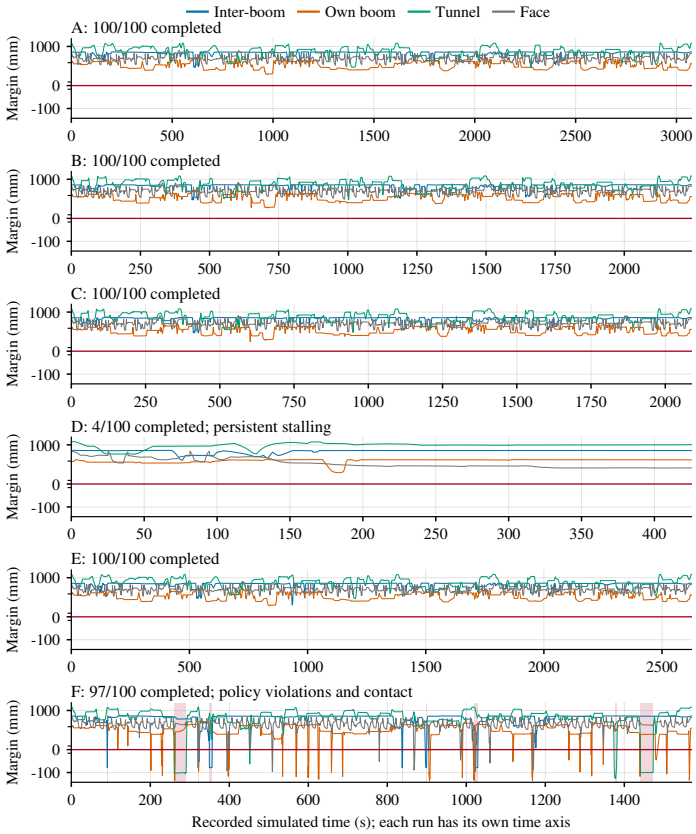

Fig. F.16. S1 clearance histories: each point retains the minimum excess over policy within a 0.1 s window, plotted at its endpoint. The symmetric logarithmic axis is linear within ±50 mm; shading marks plant-contact intervals. Time axes follow each execution. Carrier and floor minima are included in Table F.14.

Appendix F.4. Planning and computation

The plant was paused during planning, so mission durations measure synchronous simulated execution. Supervised planning required 139–167 s median computation per round on shared resources, with maximum 1497 s. Core mean/99th-percentile times for A/S1–S3 were 38.3/65.8, 41.8/71.4 and 38.1/65.2 ms. Full-framework motion/reference-duration ratios were 1.66, 1.56 and 1.66; S1 values for B/C/D/E/F were 1.06/1.05/2.54/1.43/1.16.

References

[1] T. Kivelä, J. Mattila, J. Puura, S. Launis, On-line path planning with collision avoidance for coordinate-controlled robotic manipulators, in: 2017 Bath/ASME Symposium on Fluid Power and Motion Control, ASME, 2017, paper FPMC2017-4297. doi:10.1115/FPMC2017-4297.
URL https://doi.org/10.1115/FPMC2017-4297

[2] Y. Cui, J. Pu, N. Hu, M. Cui, Smooth and efficient motion planning of large-scale and cooperative multi-arm tunnel drilling robot, Intelligence & Robotics 5 (2) (2025) 450–473. doi:10.20517/ir.2025.23.
URL https://www.oaepublish.com/articles/ir.2025.23

[3] C. Shen, C. Sloth, Safe operation for autonomous wheel loader using control barrier functions under unknown disturbances and input delay, in: 2024 IEEE 20th International Conference on Automation Science and Engineering (CASE), IEEE, 2024, pp. 4055–4061. doi:10.1109/CASE59546.2024.10711725.
URL https://doi.org/10.1109/CASE59546.2024.10711725

[4] J. Karliński, E. Rusiński, T. Lewandowski, New generation automated drilling machine for tunnelling and underground mining work, Automation in Construction 17 (3) (2008) 224–231. doi:10.1016/j.autcon.2007.05.007.
URL https://doi.org/10.1016/j.autcon.2007.05.007

[5] R. M. Molfino, R. P. Razzoli, M. Zoppi, Autonomous drilling robot for landslide monitoring and consolidation, Automation in Construction 17 (2) (2008) 111–121. doi:10.1016/j.autcon.2006.12.004.
URL https://doi.org/10.1016/j.autcon.2006.12.004

[6] M. H. Shahna, P. Mustalahti, J. Mattila, Fault-tolerant control for system availability and continuous operation in heavy-duty wheeled mobile robots, in: 2025 IEEE/ASME International Conference on Advanced Intelligent Mechatronics (AIM), IEEE, 2025, pp. 1–8.

[7] M. H. Shahna, J. Mattila, Model-free generic robust control for servo-driven actuation mechanisms with layered insight into energy conversions, in: 2025 American Control Conference (ACC), IEEE, 2025, pp. 4331–4338.

[8] M. Ortner, B. Kromoser, Influence of different parameters on drilling forces in automated drilling of concrete with industrial robots, Automation in Construction 150 (2023) 104814. doi:10.1016/j.autcon.2023.104814.
URL https://doi.org/10.1016/j.autcon.2023.104814

[9] Q. Xu, Y. Lin, Research on high-precision motion planning of large multi-arm rock drilling robot based on multi-strategy sampling rapidly exploring random tree*, Sensors 25 (9) (2025) 2654. doi:10.3390/s25092654.
URL https://www.mdpi.com/1424-8220/25/9/2654

[10] M. Heydari Shahna, T. Kivelä, J. Mattila, Pose-parameterized motion planning and CBF-QP self-collision filtering for a long-reach drilling boom, arXiv:2607.18855v1 (2026).
URL https://arxiv.org/abs/2607.18855v1

[11] A. U. Kaypak, S. Wei, P. Krishnamurthy, F. Khorrami, Safe multi-robotic arm interaction via 3D convex shapes, Robotics and Autonomous Systems 196 (2026) 105263. doi:10.1016/j.robot.2025.105263.
URL https://doi.org/10.1016/j.robot.2025.105263

[12] S. Wei, R. Khorrambakht, P. Krishnamurthy, V. M. Gonçalves, F. Khorrami, Collision avoidance for convex primitives via differentiable optimization-based high-order control barrier functions, IEEE Transactions on Control Systems Technology 34 (1) (2026) 3–18. doi:10.1109/TCST.2025.3595751.
URL https://doi.org/10.1109/TCST.2025.3595751

[13] J. Palmieri, P. Di Lillo, S. Chiaverini, A. Marino, A comprehensive control architecture for semi-autonomous dual-arm robots in agriculture settings, Control Engineering Practice 163 (2025) 106394. doi:10.1016/j.conengprac.2025.106394.
URL https://doi.org/10.1016/j.conengprac.2025.106394

[14] W. Huang, Q. Wang, S. Yang, J. Zhang, B. Xu, Adaptive sliding mode and safety control for excavators using Kinematic Control Barrier Function and sliding mode disturbance observer, Automation in Construction 172 (2025) 106046. doi:10.1016/j.autcon.2025.106046.
URL https://doi.org/10.1016/j.autcon.2025.106046

[15] D. E. J. van Wijk, D. Lee, E. Daş, T. G. Molnar, A. D. Ames, J. W. Burdick, Generalizations of backup control barrier functions: Expansion and adaptation for input-bounded safety-critical control, arXiv:2603.18450v1 (Mar. 2026). arXiv:2603.18450v1, doi:10.48550/arXiv.2603.18450.
URL https://arxiv.org/abs/2603.18450v1

[16] M. Chignoli, J.-J. Slotine, P. M. Wensing, S. Kim, URDF+: An enhanced URDF for robots with kinematic loops, in: 2024 IEEE-RAS 23rd International Conference on Humanoid Robots (Humanoids), IEEE, 2024, pp. 197–204, arXiv:2411.19753v1. arXiv:2411.19753v1, doi:10.1109/Humanoids58906.2024.10769903.
URL https://arxiv.org/abs/2411.19753v1

[17] V. Batto, L. De Matteïs, N. Mansard, Extended URDF: Accounting for parallel mechanism in robot description, in: 34th International Conference on Robotics in Alpe-Adria-Danube Region (RAAD), 2025, arXiv:2504.04767v2. arXiv:2504.04767v2.
URL https://arxiv.org/abs/2504.04767v2

[18] M. Heydari Shahna, J. Kim, J. Mattila, RoboCompiler: Graph-native compilation of closed-chain robots for consistent modeling, control, and simulation, arXiv:2609.35717v2 (Sep. 2026). arXiv:2609.35717v2, doi:10.48550/arXiv.2609.35717.
URL https://arxiv.org/abs/2609.35717v2

[19] R. Featherstone, Rigid Body Dynamics Algorithms, Springer, New York, NY, 2008.

[20] H. E. Merritt, Hydraulic Control Systems, John Wiley & Sons, 1967.

[21] E. G. Gilbert, D. W. Johnson, S. S. Keerthi, A fast procedure for computing the distance between complex objects in three-dimensional space, IEEE Journal on Robotics and Automation 4 (2) (1988) 193–203. doi:10.1109/56.2083.
URL https://doi.org/10.1109/56.2083

[22] A. D. Ames, X. Xu, J. W. Grizzle, P. Tabuada, Control barrier function based quadratic programs for safety critical systems, arXiv:1609.06408v2 (2016). doi:10.48550/arXiv.1609.06408.
URL https://arxiv.org/abs/1609.06408v2

[23] A. Agrawal, K. Sreenath, Discrete control barrier functions for safety-critical control of discrete systems with application to bipedal robot navigation, in: Proceedings of Robotics: Science and Systems, Cambridge, Massachusetts, 2017. doi:10.15607/RSS.2017.XIII.073.
URL https://www.roboticsproceedings.org/rss13/p73.html

[24] A. Singletary, Y. Chen, A. D. Ames, Control barrier functions for sampled-data systems with input delays, arXiv:2005.06418v1 (2020). doi:10.48550/arXiv.2005.06418.
URL https://arxiv.org/abs/2005.06418v1

[25] E. Todorov, T. Erez, Y. Tassa, MuJoCo: A physics engine for model-based control, in: 2012 IEEE/RSJ International Conference on Intelligent Robots and Systems, IEEE, 2012, pp. 5026–5033.

[26] D. Goldfarb, A. Idnani, A numerically stable dual method for solving strictly convex quadratic programs, Mathematical Programming 27 (1983) 1–33.